Cell Reports

Article

Whole-Cell Scale Dynamic Organization of Lysosomes Revealed by Spatial Statistical Analysis

Graphical Abstract

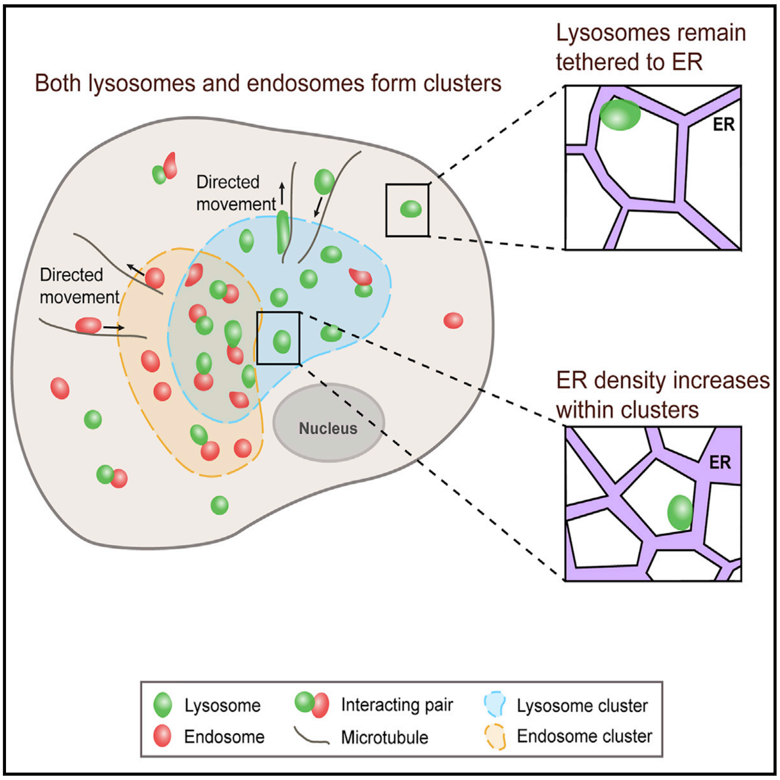

Highlights

- Lysosomes maintain non-random, stable, yet distinct spatial distributions
- Cytoskeleton, ER, and biogenesis jointly mediate lysosomal spatial distributions
- Lysosomes form dynamic clusters that increase their interactions with endosomes
- Lysosomal clustering is associated with local increases in ER spatial density

Authors

Qinle Ba, Guruprasad Raghavan, Kirill Kiselyov, Ge Yang

Correspondence

geyang@andrew.cmu.edu

In Brief

Ba et al. use spatial statistical analysis to map the whole-cell scale dynamic organization of lysosomes. Lysosomes form dynamic clusters that significantly increase their interactions with endosomes. The formation of lysosomal clusters is associated with local increases in ER spatial density but does not depend on fusion with endosomes.

Ba et al., 2018, Cell Reports *23*, 3591–3606
June 19, 2018 © 2018 The Author(s).
https://doi.org/10.1016/j.celrep.2018.05.079

CellPress

Cell Reports
Article

Whole-Cell Scale Dynamic Organization of Lysosomes Revealed by Spatial Statistical Analysis

Qinle Ba,[1] Guruprasad Raghavan,[1,4] Kirill Kiselyov,[3] and Ge Yang[1,2,5,*]
[1]Department of Biomedical Engineering, Carnegie Mellon University, Pittsburgh, PA 15213, USA
[2]Department of Computational Biology, Carnegie Mellon University, Pittsburgh, PA 15213, USA
[3]Department of Biological Sciences, University of Pittsburgh, Pittsburgh, PA 15260, USA
[4]Present address: Division of Biology and Biological Engineering, California Institute of Technology, Pasadena, CA 91125, USA
[5]Lead Contact
*Correspondence: geyang@andrew.cmu.edu

https://doi.org/10.1016/j.celrep.2018.05.079

SUMMARY

In eukaryotic cells, lysosomes are distributed in the cytoplasm as individual membrane-bound compartments to degrade macromolecules and to control cellular metabolism. A fundamental yet unanswered question is whether and, if so, how individual lysosomes are organized spatially to coordinate and integrate their functions. To address this question, we analyzed their collective behavior in cultured cells using spatial statistical techniques. We found that in single cells, lysosomes maintain non-random, stable, yet distinct spatial distributions mediated by the cytoskeleton, the endoplasmic reticulum (ER), and lysosomal biogenesis. Throughout the intracellular space, lysosomes form dynamic clusters that significantly increase their interactions with endosomes. Cluster formation is associated with local increases in ER spatial density but does not depend on fusion with endosomes or spatial exclusion by mitochondria. Taken together, our findings reveal whole-cell scale spatial organization of lysosomes and provide insights into how organelle interactions are mediated and regulated across the entire intracellular space.

INTRODUCTION

A basic strategy used by eukaryotic cells to organize their internal environment is to form specialized membrane-bound organelles such as lysosomes and endosomes. Although this strategy provides important structural and functional benefits, specialized functions of the organelles must be coordinated and integrated for cell physiology (Gottschling and Nyström, 2017). Studies have shown that different organelles interact directly and extensively through mechanisms such as membrane contact (Prinz, 2014) and membrane fusion (Martens and McMahon, 2008). Such interactions depend critically on the colocalization and, therefore, the spatial distributions of the organelles. However, we cannot explain how the interactions are mediated and regulated at the systems level within the dynamic and heterogeneous intracellular space.

To address this deficiency, we focused specifically on the lysosome, an organelle that plays essential roles in important cellular functions, such as degrading macromolecules (Luzio et al., 2007) and controlling cellular metabolism (Lim and Zoncu, 2016; Settembre et al., 2013). Within the intracellular space, lysosomes are distributed as individual compartments, and individual lysosomes are limited in their own capacity. The size of a lysosome typically is limited to several hundred nanometers (Bandyopadhyay et al., 2014; Yu et al., 2010). The number of lysosomes in a mammalian cell typically is limited to several hundred (Valm et al., 2017). Furthermore, lysosomes are specialized compartments that depend on interactions with partner organelles to fulfill their functions (Bonifacino and Neefjes, 2017; Luzio et al., 2007). For example, they depend on fusion with endosomes and autophagosomes to receive and degrade materials from the endocytic and autophagic pathways, respectively (Eskelinen and Saftig, 2009; Luzio et al., 2007). Given the functional limitations of individual lysosomes, a fundamental yet unanswered question is whether and, if so, how individual lysosomes are organized in the intracellular space so that their functions can be coordinated and integrated to meet the changing needs of cells. Answering this question is key to elucidating how lysosomes function at the systems level in single cells.

Recent studies on the positioning of lysosomes (Bonifacino and Neefjes, 2017; Pu et al., 2016) have begun to reveal their spatial organization within the intracellular space. Positioning of individual lysosomes is mediated by mechanisms that include their active transport along microtubules and their interactions with the actin cytoskeleton and partner organelles, especially the ER (Bonifacino and Neefjes, 2017; Pu et al., 2016; Valm et al., 2017). Under normal conditions, lysosomes in non-polarized mammalian cells often cluster in a perinuclear region surrounding the microtubule-organizing center (MTOC), forming what is called the perinuclear cloud (Jongsma et al., 2016; Korolchuk et al., 2011; Pu et al., 2016), but they also spread into peripheral regions of cells, with some approaching the plasma membrane. This spatial pattern provides direct evidence for the spatial organization of individual lysosomes, and a wide variety of perturbations can change this pattern (Pu et al., 2016). For example, nutrient deprivation substantially increases the fraction of lysosomes clustering in the perinuclear region and decreases the fraction of lysosomes spreading into peripheral regions. Nutrient recovery reverses these changes and restores the usual pattern of lysosomal distribution (Korolchuk et al., 2011; Li et al., 2016). The relocation of lysosomes under these conditions is mediated by motor-mediated active transport along microtubules, and the underlying molecular machineries and mechanisms have begun to be elucidated (Korolchuk et al., 2011; Li et al., 2016; Pu et al., 2015). Functions of lysosomal positioning in mediating cellular nutrient response (Korolchuk et al., 2011) and regulating lysosomal degradative capacity (Johnson et al., 2016) also have begun to be elucidated. Despite these advances, related studies have a basic limitation in elucidating the spatial organization of lysosomes in that they lack quantitative and comprehensive characterization and analysis of the collective behavior of lysosomes, especially at the whole-cell scale.

That subcellular structures such as organelles and proteins exhibit defined spatial patterns has been noted in many studies (e.g., Boland and Murphy, 2001; Glory and Murphy, 2007; Valm et al., 2017). These patterns reflect the spatial organization of the subcellular structures and have been characterized and analyzed using pattern recognition and machine learning techniques (Boland and Murphy, 2001; Johnson et al., 2015). However, the specific modes, molecular mechanisms, and cellular functions of these patterns remain poorly understood.

In this study, we probed the spatial organization of lysosomes in cultured COS-7, U2OS, or BS-C-1 cells. Our overall strategy was to study the collective behavior of lysosomes, especially their spatial distributions at the whole-cell scale, using spatial statistical analysis techniques. Specifically, we treated the spatial distribution of lysosomes in a single cell mathematically as a spatial point process and analyzed it using related statistical techniques (Baddeley et al., 2016; Diggle, 2014; Illian et al., 2008). Our findings identified specific modes, molecular mechanisms, and cellular functions of the spatial organization of lysosomes at the whole-cell scale and provided insights into how cells organize their organelles and mediate their interactions.

RESULTS

Lysosomes Maintain Non-random, Stable, and yet Distinct Spatial Distributions in Single Cells

To investigate whether and, if so, how lysosomes are spatially organized, we analyzed their spatial distributions at the whole-cell scale in live BS-C-1 cells, chosen for their flat profiles to facilitate imaging. We labeled lysosomes using dextran Alexa Fluor 488 and a collected time-lapse videos at 4 frames per second for 1 min (Experimental Procedures; Figure 1A; Video S1). Because most of the lysosomes in single BS-C-1 cells resided in a single focal plane, we treated their spatial distributions as two dimensional for simplification. Within each cell we analyzed, we observed extensive movement of lysosomes throughout the intracellular space, with many traversing long distances for the duration of imaging (Figure 1B; Video S1). For each cell we analyzed, we detected individual lysosomes as single particles (Supplemental Experimental Procedures). We then considered their spatial distribution mathematically as a two-dimensional spatial point process and analyzed it using related spatial statistical techniques (Baddeley et al., 2016; Diggle, 2014; Illian et al., 2008). Specifically, we checked whether the lysosomes were randomly distributed by complete spatial randomness (CSR) tests (Supplemental Experimental Procedures) at different time points. We found that the spatial distribution of lysosomes differed substantially from a random distribution at all of the time points we analyzed (Figures 1C–1E), indicating that lysosomes are spatially organized at the whole-cell scale.

To quantitatively characterize the spatial distribution of lysosomes at the whole-cell scale, we used three statistical distance distributions (Figures S1A–S1C; Supplemental Experimental Procedures). We calculated these distributions every 5 s in each cell to examine their variations over time (Figures 1F–1H). First, we quantified the positioning of all of the lysosomes relative to one another in each cell using the distribution of their normalized pairwise distances (Figure S1A), referred to as the normalized inter-organelle distance distribution (Diggle, 2014). For the cell shown in Figures 1A and 1B, this distribution remained generally stable for the duration of imaging; the profile spread broadly but showed a characteristic peak spacing at ~0.35 (Figure 1F). The distributions in other cells that we analyzed showed similar stability and comparable but different profiles (Figures S1D, S1E, and S2A, blue lines). Second, we quantified the positioning of all of the lysosomes relative to the nucleus using the distribution of their normalized shortest distances to the nucleus (Figure S1B), referred to as the normalized to-nucleus distance distribution. For the cell shown in Figures 1A and 1B, this distribution also remained generally stable, but its profile showed two characteristic peak distances, at ~0.3 and ~0.9, respectively (Figure 1G). The distributions in other cells showed similarly stable but remarkably diverse profiles (Figures S1D, S1E, and S2B, blue lines). Third, we quantified the level of crowding of the lysosomes in each cell (i.e., how closely they are spaced) using the distribution of their nearest-neighbor distances (Figure S1C), referred to as the nearest-neighbor distance distribution (Baddeley et al., 2016; Diggle, 2014; Illian et al., 2008). For the cell shown in Figures 1A and 1B, this distribution also remained stable and showed a characteristic peak distance at ~1 μm (Figure 1H). The distributions in other cells showed similar stability and profiles (Figures S1D, S1E, and S2C, blue lines). Together, the three distance distributions provide a comprehensive characterization of the spatial distribution of lysosomes at the whole-cell scale.

We have noted that the three distance distributions remained generally stable for the duration of imaging in each cell that we analyzed. To characterize the stability of each distribution, we quantified its variations over time using the Sørensen dissimilarity score between its profiles at any two different time points (Supplemental Experimental Procedures). For the cell shown in Figures 1A and 1B, the average dissimilarity score was 3.29% for the normalized inter-organelle distance distribution, 2.65% for the normalized to-nucleus distance distribution, and 5.80% for the nearest-neighbor distance distribution (Figures 1F–1H). Examination of these distributions in different cells (Figures S1D and S1E) and for different durations of imaging (Figures S1F and S1G) found similarly low levels of variations. Lastly, we compared the three distance distributions of lysosomes in

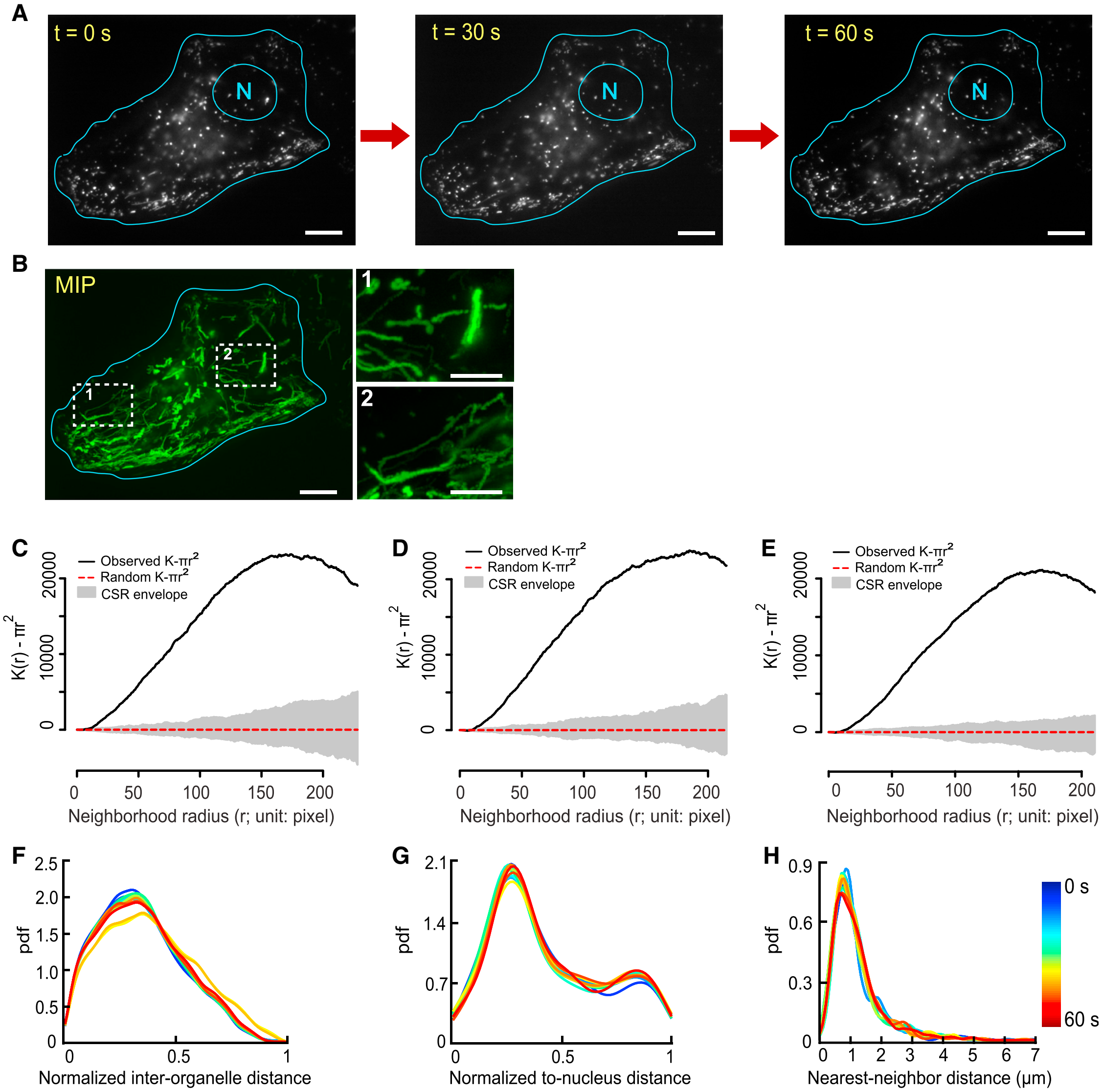

Figure 1. Lysosomes Maintain Non-random and Stable Spatial Distributions in a Single Cell

(A) Lysosomes in a BS-C-1 cell at three selected time points. N, nucleus. Scale bars, 10 μm.

(B) Maximum intensity projection (MIP; green) of lysosomal movement for 1 min, imaged at 4 frames per second. Each trace corresponds to the trajectory of a lysosome. Scale bar, 10 μm. Scale bars in insets, 5 μm.

(C–E) Complete spatial randomness (CSR) test of whole-cell scale lysosomal distribution at the three time points in (A). (C) 0 s; (D) 30 s; (E) 60 s. Adjusted Ripley's *K*-function of lysosomes within the cell (solid black line). Adjusted Ripley's *K*-function of a random distribution within the same cell boundary (dotted red line). Uncertainty envelope for the random distribution (gray area). The extent of separation between the solid black line and the CSR envelope indicates how close the spatial distribution of lysosomes is to a random distribution.

(F–H) Three distance distributions of lysosomes, color coded based on time and plotted every 5 s for 60 s. Their temporal variations were quantified using Sørensen dissimilarity scores. Because the distributions at 0, 5, 10, … 60 s were selected, 13 distributions were compared pairwise, hence $C_{13}^{2} = 78$ pairs. pdf, probability density function. Temporal variations (means ± SDs; n = 78): (F) 3.29% ± 2.98%; (G) 2.65% ± 0.92%; (H) 5.80% ± 1.48%.

different cells (Figures S2A–S2C, blue lines) in a pairwise fashion (Supplemental Experimental Procedures). We found that the distributions differed significantly in all or most of the comparisons (Figure S2D, "unpatterned" columns). We checked and confirmed that the distinct spatial distributions of lysosomes in single cells were not merely a secondary effect of distinct cell shapes (Supplemental Experimental Procedures; Figure S2; Video S2). Taken together, our data show that although lysosomes undergo extensive long-distance movement across the entire intracellular space, they maintain non-random, stable, yet distinct spatial distribution in single cells. This reveals not only homeostasis in the positioning of lysosomes relative to one another and to the nucleus in the same cell but also heterogeneity in the positioning among different cells. This further indicates that lysosomes are spatially organized at the whole-cell scale.

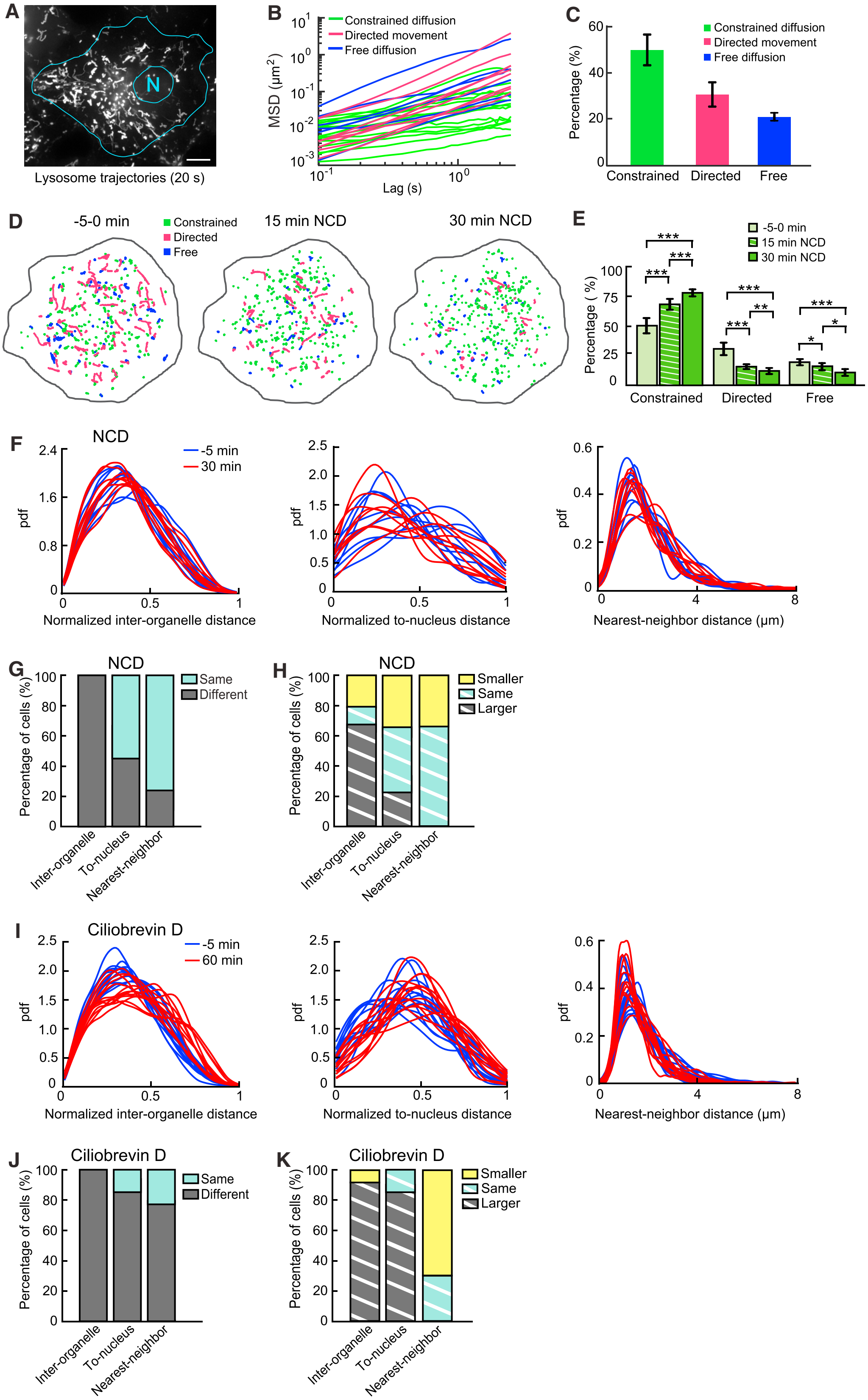

(legend on next page)

Lysosomes in a Single Cell Form Different Subpopulations

Thus far we have focused on the spatial distribution of the entire population of lysosomes in single cells. However, it is clear even from a simple visual inspection that the population is heterogeneous in its dynamic behavior; while some lysosomes traverse long distances, others seem constrained in their movement (Figure 2A; Video S1). This raises the important question of how lysosomes with different behaviors together maintain the stable spatial distribution of their whole population. To answer this question, we first examined the composition of the lysosomal population in COS-7 cells by tracking individual lysosomes as single particles and characterizing their behavior through mean square displacement (MSD) analysis (Figures 2B and 2C) (Qian et al., 1991; Saxton, 1997). We found that on average, ~49% of lysosomes in a single cell underwent constrained diffusion, ~31% underwent directed movement, and ~20% underwent free diffusion (Figure 2C). This shows that most lysosomes undergo either constrained diffusion or directed movement, while only a small fraction undergoes free diffusion, which is consistent with the finding in previous studies that free diffusion is limited inside cells (Bandyopadhyay et al., 2014; Luby-Phelps et al., 1988).

Sustained and Balanced Transport along Microtubules Is Required to Maintain Population Composition and Spatial Distributions of Lysosomes

After determining the composition of the lysosomal population, we investigated its relation to microtubule-based active transport. To this end, we depolymerized the microtubule cytoskeleton by treating COS-7 cells with 2.5 μM of nocodazole. After 30 min of treatment, the fraction of lysosomes undergoing directed movement was reduced significantly, from 31% to 12%. The fraction of lysosomes undergoing constrained diffusion was increased significantly, from 49% to 77%. The fraction of lysosomes undergoing free diffusion was reduced significantly, from 20% to 11% (Figures 2D and 2E). This shows that sustained microtubule-based transport is required to maintain the population composition of lysosomes.

Because microtubule-based active transport is crucial to the positioning and relocation of lysosomes (Bonifacino and Neefjes, 2017; Pu et al., 2016), we reason that it should play an important role in maintaining the stable spatial distributions of lysosomes. To test this hypothesis, we compared the three distance distributions of the lysosomes right before and 30 min after the nocodazole treatment (Figure 2F). We found that although inhibition of the transport caused significant changes in the normalized inter-organelle distance distribution in all of the cells we analyzed (Figure 2G), it did not consistently decrease or increase the median distance (Figure 2H). The normalized to-nucleus distance distribution remained unchanged in ~56% of the cells (Figure 2G), and inhibition of the transport did not consistently decrease or increase its median distance (Figure 2H). Furthermore, the nearest-neighbor distance distribution and its median remained unchanged in the majority of the cells (Figures 2G and 2H), indicating that microtubule-based transport does not play a major role in maintaining the crowding of lysosomes.

We hypothesize that the lack of consistent changes in the median normalized inter-organelle distance and the median normalized to-nucleus distance after nocodazole treatment is because the centrifugal transport and centripetal transport of the lysosomal population are balanced. Abolishing the entire transport process by nocodazole treatment would not shift the balance consistently in either direction. To test this hypothesis, we treated the cells (plural form) with dynein inhibitor ciliobrevin D (Firestone et al., 2012), which disrupts primarily the centripetal movement and shifts the balance toward the centrifugal movement. We found that inhibiting dynein-mediated transport caused significant changes in the three distance distributions in all or most of the cells analyzed (Figures 2I–2K). It also consistently increased the median normalized to-nucleus distance and the median normalized inter-organelle distance in most of the cells and decreased the median nearest-neighbor distance in the majority of cells (Figures 2I–2K). Taken together, our findings

Figure 2. Composition of the Lysosomal Population and Roles of Microtubule-Based Active Transport in Maintaining Its Stable Spatial Distribution

(A) Maximum intensity projection of movement of lysosomes in a COS-7 cell imaged at 10 frames per second for 20 s. Scale bar, 15 μm.

(B) MSD of randomly selected 10% of all lysosomal trajectories.

(C) Percentage of each subpopulation (means ± SDs; n = 9 cells): constrained: 49.41% ± 6.24%; directed: 30.94% ± 5.40%; free: 19.64% ± 2.19%. Error bars indicate SD.

(D) Color-coded trajectories of lysosomes at three time points in a cell treated with 2.5 μM nocodazole (NCD).

(E) Changes in lysosomal subpopulations under NCD treatment over time (means ± SDs; n = 9 cells). Constrained (0, 15, and 30 min): 49.41% ± 6.24%, 67.74% ± 4.17%, and 77.20% ± 3.32%, respectively. Directed (0, 15, and 30 min): 30.94% ± 5.40%, 16.77% ± 2.05%, and 11.71% ± 2.48%, respectively. Free (0, 15, and 30 min): 19.65% ± 2.19%, 15.49% ± 3.32%, and 11.05% ± 3.80%, respectively. Comparison of pooled data from the same cells before and after NCD treatment. p values (0 min versus 15 min, 0 min versus 30 min, and 15 min versus 30 min): constrained: 1.8×10^{-4}, 9.6×10^{-6}, and 8.1×10^{-4}, respectively; directed: 2.7×10^{-5}, 3.2×10^{-5}, and 2.0×10^{-3}, respectively; free: 2.6×10^{-2}, 7.3×10^{-5}, and 1.3×10^{-2}, respectively. *$p < 0.05$; **$p < 0.01$; ***$p < 0.001$. Error bars indicate SD.

(F) The three distance distributions before and after 30 min of NCD treatment in 9 different cells.

(G) Comparison of different distance distributions of lysosomes before versus after NCD treatment. Cutoff p value for statistical significance: 0.05. Inter-organelle (same, different): 0%, 100%, respectively; to-nucleus: 55.5%, 44.4%, respectively; and nearest-neighbor: 77.8%, 22.2%, respectively.

(H) Comparison of median distances before versus after NCD treatment. Inter-organelle (smaller, same, and larger): 22.2%, 11.1%, and 66.7%, respectively; To-nucleus: 33.3%, 44.4%, and 22.2%, respectively; and nearest-neighbor: 33.3%, 66.7%, and 0%, respectively.

(I) The three distance distributions before and after 1 hr of ciliobrevin D (80 μM) treatment in 13 different cells.

(J) Comparison of three distance distributions before versus after ciliobrevin D treatment of the same cells: Inter-organelle (same, different): 0%, 100%, respectively; to-nucleus: 15.4%, 84.6%, respectively; and nearest-neighbor: 23.1%, 76.9%, respectively.

(K) Comparison of median distances before versus after ciliobrevin D treatment. Inter-organelle (smaller, same, larger) 7.7%, 0%, 92.3%, respectively; To-nucleus: 0%, 15.4%, 84.6%, respectively; Nearest-neighbor: 69.2%, 30.8%, 0%, respectively.

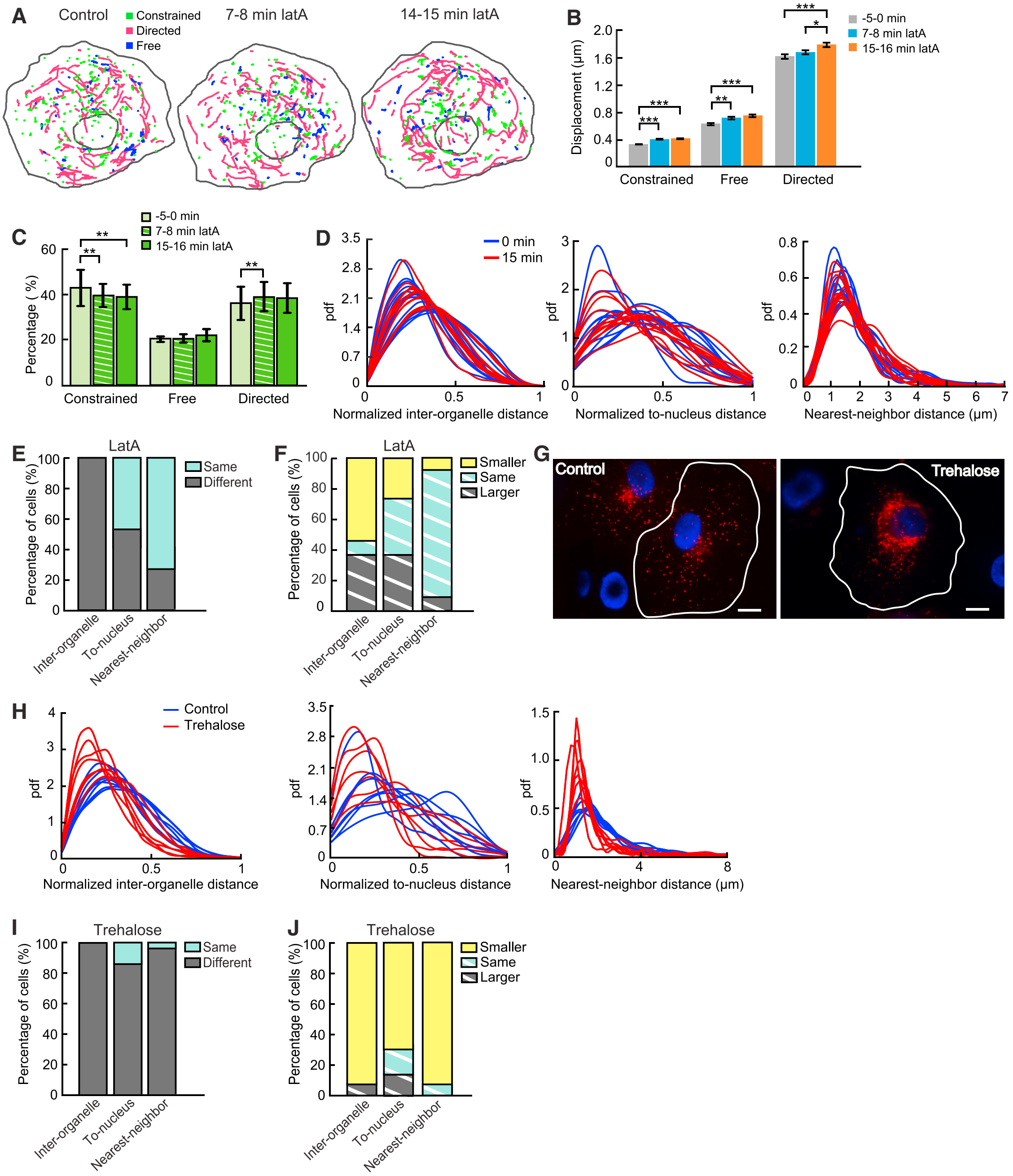

Figure 3. Roles of Interaction with the Actin Cytoskeleton and Lysosomal Biogenesis in Maintaining Subpopulations and Spatial Distributions of Lysosomes

(A) Color-coded trajectories of lysosomes in COS-7 cells treated with 0.8 µM latA. Videos were collected at 10 frames per second for 20 s.

(B) Changes in the displacement for 5 s of the three subpopulations under latA treatment. Comparison of pooled data from the same 11 cells before and after treatment. Constrained diffusion: 0.32 ± 0.0058 µm (mean ± SEM; 0 min, n = 2,052 trajectories), 0.39 ± 0.0076 µm (7.5 min, n = 1,821), and 0.41 ± 0.0075 µm (15 min, n = 1,747). Free diffusion: 0.57 ± 0.019 µm (0 min, n = 688 trajectories), 0.66 ± 0.020 µm (7.5 min, n = 633), and 0.68 ± 0.019 µm (15 min, n = 675). Directed movement: 1.61 ± 0.031 µm (0 min, n = 1,757 trajectories), 1.67 ± 0.031 µm (7.5 min, n = 1,833), and 1.78 ± 0.032 µm (15 min, n = 1,713). p values (0 min versus 7.5 min, 0 min versus 15 min, and 7.5 min versus 15 min): constrained diffusion: 1.2×10^{-14}, 1.9×10^{-22}, and 0.083, respectively; free diffusion: 2.1×10^{-3}, 3.6×10^{-5}, and 0.32, respectively; directed movement: 0.17, 1.6×10^{-4}, and 0.014, respectively. Error bars indicate SEM.

(C) Changes in the three subpopulations under latA treatment over time (means ± SDs; n = 11 cells). Constrained (0, 7.5, and 15 min): 42.14% ± 6.90%, 39.34% ± 5.09%, and 38.96% ± 5.60%, respectively. Free: 20.34% ± 1.31%, 20.41% ± 1.68%, and 21.74% ± 2.51%, respectively. Directed: 37.52% ± 7.02%, 40.25% ± 6.00%, and 39.30% ± 6.20%, respectively. p values (0 min versus 7.5 min, 0 min versus 15 min, and 7.5 min versus 15 min): constrained: 0.0058, 0.0053, and 0.49, respectively; free: 0.98, 0.15, and 0.22, respectively; directed: 0.0043, 0.10, and 0.61, respectively. Error bars indicate SD.

(legend continued on next page)

indicate that the balance between centrifugal and centripetal transport is required to maintain stable spatial distributions of lysosomes. Because of this balance, lysosomes can undergo long-distance transport without affecting their overall stable spatial distributions at the whole-cell scale.

Interaction with the Actin Cytoskeleton Is Required to Constrain Diffusion of Lysosomes and to Maintain Their Positioning Relative to One Another

We have shown that microtubule-based transport is required to maintain the lysosomal subpopulation undergoing directed movement. This raises the question of what maintains the subpopulation undergoing constrained diffusion. Interaction of lysosomes with the actin cytoskeleton plays an important role in mediating their positioning (Bonifacino and Neefjes, 2017; Pu et al., 2016). In particular, interaction with the cortical actin network has been shown to transiently constrain lysosomes near the cell periphery (Caviston et al., 2011; Encarnação et al., 2016). We hypothesize that interaction with the actin cytoskeleton is required for maintaining the subpopulation of lysosomes undergoing constrained diffusion.

To test this hypothesis, we depolymerized the actin cytoskeleton by treating cells with 0.8 μM latrunculin A (latA). We confirmed the effectiveness of the treatment based on the changes in cell shapes (Figure S3A) and the reduction of polymerized actin levels (Figures S3B and S3C). To avoid complications in result interpretation, we chose to analyze cells without substantial changes in their shapes. To determine how depolymerization of the actin cytoskeleton affected the three lysosomal subpopulations, we compared their mean displacement in 5 s immediately before the treatment and 15–16 min after the treatment (Figures 3A and 3B). We observed significant increases in mean displacements of all three subpopulations (Figures 3B and S3D). Despite these significant changes, the fractions of lysosomes undergoing constrained diffusion and directed movement were changed only slightly, from 42.1% to 38.9% and from 37.5% to 39.3%, respectively (Figure 3C). The fraction of lysosomes undergoing free diffusion remained unchanged (Figure 3C). Taken together, our data show that although the actin cytoskeleton constrains diffusion and directed movement of lysosomes, it plays only a minor role in maintaining the population composition of lysosomes.

Next, we investigated the role of the actin cytoskeleton in maintaining the spatial distribution of lysosomes. To this end, we compared the three distance distributions of lysosomes right before and 15–16 min after the latA treatment (Figure 3D). We found that depolymerization of the actin cytoskeleton caused significant changes in the normalized interorganelle distance distribution, the normalized to-nucleus distance distribution, and the nearest-neighbor distance distribution in 100%, ~55%, and ~25% of the cells, respectively (Figure 3E). In addition, we found that depolymerization of the actin cytoskeleton did not result in a consistent increase or decrease in the median distances of lysosomes relative to one another and to the cell nucleus (Figure 3F). The median nearest-neighbor distance was unchanged in most of the cells (Figure 3F). We reason that this is because interaction with the actin cytoskeleton does not alter the balance between the centrifugal and the centripetal transport of lysosomes. Taken together, our results indicate that interaction with the actin cytoskeleton is required to maintain the positioning of lysosomes relative to one another but plays a minor role in maintaining their positioning relative to the nucleus and their crowding.

A Stable Level of Lysosomal Biogenesis Is Required to Maintain a Stable Spatial Distribution of Lysosomes

We have thus far investigated the roles of the cytoskeleton in mediating the population composition and spatial distributions of lysosomes. Upregulation or downregulation of lysosomal biogenesis also can cause substantial changes in the spatial distribution of lysosomes (Jongsma et al., 2016; Korolchuk et al., 2011; Pu et al., 2016; Sardiello et al., 2009), but such changes have not been quantitatively characterized at the whole-cell scale. To investigate how an altered level of lysosomal biogenesis may influence the stable spatial distributions of lysosomes, we treated COS-7 cells with 50 mM trehalose (Sarkar et al., 2007), which activates TFEB, the master regulator of lysosomal biogenesis (Sardiello et al., 2009; Settembre et al., 2011). We found that trehalose treatment substantially increased the fraction of lysosomes clustering in the perinuclear region (Figure 3G) and significantly decreased the distances between lysosomes and between lysosomes and the cell nucleus (Figures 3H–3J), in agreement with the observations of previous studies (Sardiello et al., 2009; Settembre et al., 2011). In addition, the treatment significantly increased crowding of lysosomes as the median nearest-neighbor distance was reduced by ~29%, substantially stronger in effect than the perturbations to the cytoskeleton analyzed previously (Figures 2F, 2I, and 3D). Treatment of COS-7 cells with 2 μM torin 1, a potent and selective ATP-competitive inhibitor of mechanistic target of rapamycin (mTOR) (Thoreen et al., 2009), also substantially increased the fraction of lysosomes clustering in the perinuclear region

---

(D) The three distance distributions before and 15 min after latA treatment in 11 cells.

(E) Comparison of distributions before and after latA treatment (n = 55 pairs). Inter-organelle (same, different): 0%, 100%, respectively; to-nucleus: 45.5%, 54.5%, respectively; nearest-neighbor: 72.7%, 27.3%, respectively.

(F) Comparison of median distances before and after latA treatment (n = 55 pairs). Inter-organelle (smaller, same, and larger): 54.5%, 9.1%, and 36.4%, respectively; to-nucleus: 27.3%, 36.4%, and 36.4%, respectively; nearest-neighbor: 9.1%, 81.8%, and 9.1%, respectively.

(G) Comparison of lysosomal spatial distributions in a control cell (left) versus a cell treated with trehalose (right; 50 mM, 12 hr). Lysosomes (red); nuclei (blue). Scale bars, 15 μm.

(H) The three distance distributions in control cells (n = 7) versus trehalose-treated cells (12 hr, 7 cells).

(I) Comparison of distributions in control cells versus cells treated with trehalose (n = 49 pairs). Inter-organelle (same, different): 0%, 100%, respectively; to-nucleus: 14.3%, 85.7%, respectively; nearest-neighbor: 2.1%, 97.9%, respectively.

(J) Comparison of median distances in control cells versus cells treated with trehalose (n = 49 pairs). Inter-organelle (smaller, same, and larger): 91.8%, 0%, and 8.2%, respectively; to-nucleus: 69.4%, 16.3%, and 14.3%, respectively; nearest-neighbor: 91.8%, 8.2%, and 0%, respectively.

(Figures S4A–S4C) and the localization of TFEB to the nucleus (Figures S4D and S4E). The distances between lysosomes and between lysosomes and the cell nucleus were significantly decreased in ~50% of the comparisons (Figures S4F, S4G, S4I, and S4J), similar to those under trehalose treatment. However, the median nearest-neighbor distance was increased by 36% (Figures S4H–S4J). Together, these results show that a stable level of lysosomal biogenesis is required to maintain a stable spatial distribution of lysosomes and that different perturbations of lysosomal biogenesis by trehalose and torin 1 treatment lead to differential changes in spatial distributions of lysosomes.

Lysosomes Form Dynamic Clusters throughout the Intracellular Space

We have shown that lysosomes are spatially organized at the whole-cell scale because their spatial distributions are non-random, stable, yet distinct in single cells. Here, we further investigate how they are organized spatially. A common pattern in the spatial distributions of lysosomes is their clustering in the perinuclear region (Jongsma et al., 2016; Korolchuk et al., 2011; Pu et al., 2016), defined by their substantially higher spatial density than in neighboring areas. This raises the question of whether lysosomes cluster in other intracellular regions. To answer this question, we plotted their spatial density across the entire intracellular space (Figures 4A and 4B; Supplemental Experimental Procedures). The plots revealed that lysosomes formed clusters throughout the intracellular space, which could be identified visually by their elevated spatial densities (Figures 4A and 4B; Video S3). To identify these clusters computationally, we used the Density-Based Spatial Clustering of Applications with Noise (DBSCAN) algorithm (Ester et al., 1996) (Supplemental Experimental Procedures). We found that lysosomal clusters were dynamic and underwent turnover activities such as merging, splitting, appearance, and disappearance (Figures 4C and S5A).

To quantitatively characterize the lysosomal clusters, we first examined their composition and found that on average, 47.9% of their members underwent constrained diffusion, 30.6% underwent directed movement, and 21.5% underwent free diffusion (Figure 4D), consistent with the composition of the entire lysosome population (Figure 2C) but more heterogeneous given its larger variations (Figure 4D). We then quantified the sizes of the clusters by their numbers of lysosomes and areas. We found that the median number of lysosomes of the clusters was 8, with the maximum reaching ~200 (Figure 4E). The median area of the clusters was 13.3 μm^2, with the maximum reaching ~1,084 μm^2 (Figure S5B). Lastly, we examined the lifetime of the clusters by following randomly selected clusters over time. We found that the average lifetime of the clusters was 10.9 ± 1.3 s (mean ± SEM; n = 30 clusters from 9 cells), with the maximum reaching ~20 s.

To determine the mechanisms underlying the formation and dynamic turnover of lysosomal clusters, we combined single-particle tracking analysis (Figures 2B and 2C) with clustering analysis (Figure S5C; Video S4). We found that the *de novo* formation of a new cluster at a certain location was mediated jointly by incoming lysosomes undergoing either directed movement or free diffusion with lysosomes undergoing constrained diffusions at the location (Figure S5C; Video S4). This finding is consistent with the measured properties of the clusters. The mean lifetime of a cluster is ~11 s. Within this time interval, the mean displacement of a lysosome undergoing constrained diffusion is <0.5 μm. Because the median diameter of a cluster is 4.23 μm (Figure S5B), formation of a new cluster requires long-range inward transport of lysosomes undergoing either directed movement or free diffusion (Figure S5C). Because only a small fraction of lysosomes undergoes free diffusion (Figure 2C), we conclude that cluster formation is mediated primarily by incoming lysosomes undergoing directed movement together with local lysosomes undergoing constrained diffusion. Our single-particle tracking provided no evidence that newly synthesized lysosomes appeared in the clustering region. Consistent with our finding on cluster formation, we found that dynamic turnovers of lysosomal clusters were mediated primarily by long-range movements of lysosomes, especially those undergoing directed movement. To further test this finding, we compared the lifetime of clusters in control cells versus cells treated with nocodazole. We found a significant increase in their mean lifetime by ~73% (Figure 4F), which supports our finding.

Formation of Lysosomal Clusters Is Associated with Local and Significant Increases in ER Spatial Density

A substantial fraction of lysosomes remained constrained in their diffusion after depolymerization of the actin network (Figure 3C). This indicates that other mechanisms contribute to the constraining of lysosomal diffusion. Because the ER network extends throughout the intracellular space and interacts with lysosomes (Bonifacino and Neefjes, 2017; Pu et al., 2016; Valm et al., 2017), we hypothesize that it constrains lysosomal diffusion. To test this hypothesis, we imaged ER and lysosomes simultaneously (Figure 5A; Supplemental Experimental Procedures). Consistent with previous reports (Friedman et al., 2013; Raiborg et al., 2015; Valm et al., 2017), we found that lysosomes remained constantly tethered to ER (Figure 5A; Video S5). Lysosomes confined to the ER network exhibited a variety of behaviors, including directed movement along ER tubules (Figures 5A and 5B), constrained diffusion (Figures 5A and 5C), or association with the tips of growing ER tubules (Figure 5A). Consistent with findings by Valm et al. (2017), some lysosomes exhibited free diffusion while confined by ER (Figure 5D).

Given that lysosomes remain constantly tethered to the ER network, we probed its role in lysosomal cluster formation by comparing its spatial density within the clusters versus within non-cluster regions (Figure 5E; Supplemental Experimental Procedures). We found that the formation of the clusters is associated with local and significant increases in ER density within the clusters (Figure 5F), indicating that the ER may play a direct role in mediating cluster formation.

Formation of Lysosomal Clusters Does Not Depend on Spatial Exclusion or Restriction by Mitochondria

Mitochondria occupy a substantial fraction of the intracellular space in many cell types. For example, ~22% of the volume of a liver cell is occupied by mitochondria (Alberts et al., 2014). Within the intracellular space, mitochondria often form aggregates, which can exclude and restrict lysosomes spatially. This

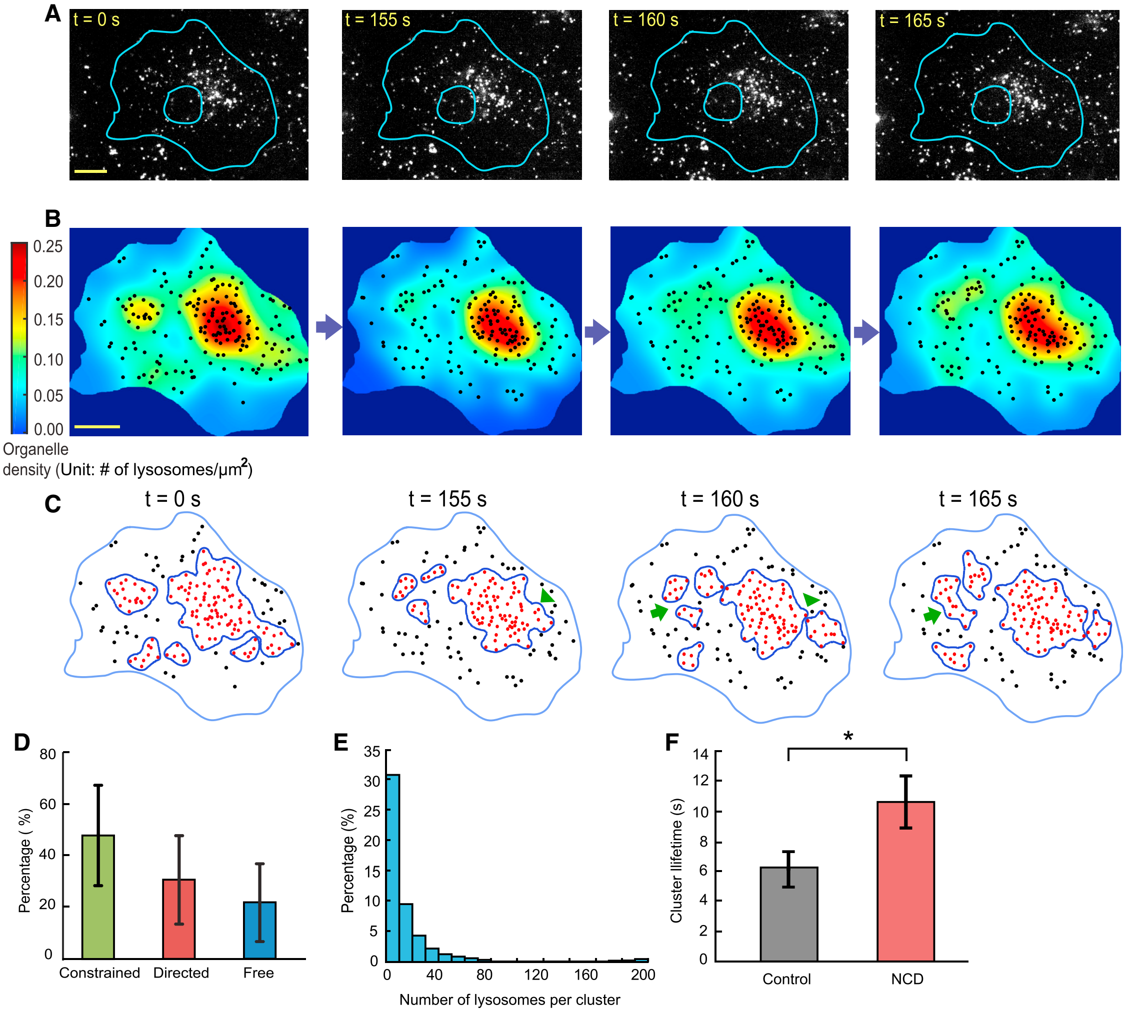

Figure 4. Lysosomes Form Dynamic Clusters throughout the Intracellular Space

(A) Selected frames from a time-lapse video of lysosomes in a COS-7 cell. Scale bar, 20 μm.

(B) Color-coded spatial density plots of lysosomes calculated for the frames shown in (A). Scale bar, 20 μm.

(C) Clusters of lysosomes identified computationally by DBSCAN. Arrowheads point to cluster-splitting sites. Arrows point to cluster-merging sites.

(D) Composition of clusters, calculated for each cluster and then pooled for analysis. Constrained diffusion 47.9% ± 19.7%; directed movement, 30.6% ± 17.7%; free diffusion, 21.5% ± 14.9% (means ± SDs; n = 376 clusters from 9 cells, within 5 frames randomly selected from each cell). Error bars indicate SD.

(E) Size distribution of clusters, measured by their numbers of lysosomes. Same clusters from the same cells as those in (D). The average number of lysosomes was 15.4 ± 1.3 per cluster (means ± SEMs; n = 376 clusters from 9 cells). The median number of lysosomes was 8.

(F) Lifetime of large clusters with >10 lysosomes in the same cells before and after NCD treatment, as shown in Figure 2D. Before NCD treatment, 6.14 ± 1.22 s (mean ± SEM; n = 34 clusters from 8 cells); after NCD treatment, 10.69 ± 1.76 s (mean ± SEM; n = 24 clusters from 8 cells); p = 0.013. Error bars indicate SEM.

raises the question of whether clustering of lysosomes is merely a secondary outcome of the cellular crowding of mitochondria and their spatial exclusion and restriction of lysosomes. To address this question, we imaged mitochondria and lysosomes simultaneously in COS-7 cells and examined their spatial relations (Figures 5G–5I). In regions not occupied by mitochondria, we frequently observed formation, turnover, and dispersion of lysosomal clusters (Figures 5J–5L; Video S6). This indicates that spatial exclusion or restriction of lysosomes by mitochondria is not a necessary condition for lysosomal clustering. In regions that are densely occupied by mitochondria, such as the perinuclear region, some lysosomes appeared to be excluded or constrained in their movement by surrounding mitochondria, but many others did not appear to be affected because their movement showed no apparent correlation with the movement of mitochondria in close proximity (Video S6). This is not surprising, given that the movement of lysosomes is confined by the ER network. In those regions that are densely occupied by mitochondria, clusters of lysosomes were frequently observed, many undergoing dynamic changes without apparent correlation with the movement of neighboring mitochondria (Video S6). Taken together, these results indicate that the clustering of lysosomes does not depend on their spatial exclusion or restriction by mitochondria and therefore is not merely a secondary

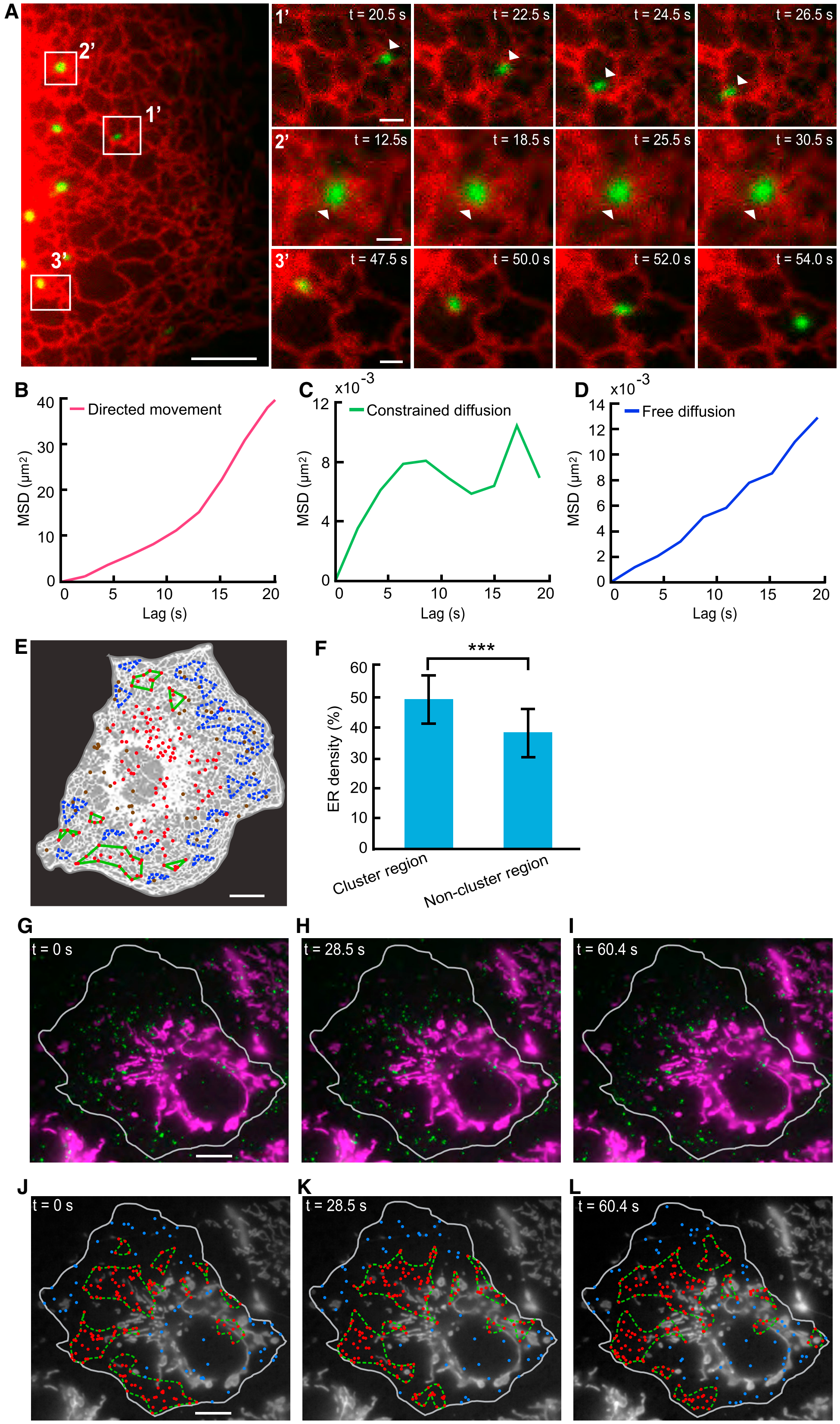

(legend on next page)

outcome, even though the spatial exclusion or restriction may contribute to the clustering.

Clustering of Lysosomes Significantly Increases Their Interaction with Late Endosomes

That lysosomes form dynamic clusters throughout the intracellular space raises the important question of what cellular functions these clusters may serve. Previous studies have assumed that the clustering of lysosomes in the perinuclear region when cells are under stress promotes their interactions with partner organelles such as autophagosomes (Jongsma et al., 2016; Korolchuk et al., 2011; Pu et al., 2016), but this assumption has not been directly tested. Here, we make a similar hypothesis, namely under normal conditions, that clusters of lysosomes throughout the intracellular space increase interactions of lysosomes with partner organelles because of their increased lysosomal spatial density. To directly test this hypothesis, we imaged lysosomes and late endosomes concurrently at approximately 5 s per frame for 5 min (Figure 6A; Video S7) and then analyzed their interactions. First, we confirmed that our experimental assay could reliably differentiate between lysosomes and late endosomes (Figure S6A; Supplemental Experimental Procedures). Then, we developed a computational method that identifies pairs of lysosomes and endosomes with a high likelihood of interacting with one another. Specifically, we identified a lysosome and an endosome as an interacting pair if they maintained a center distance below a threshold ranging from 400–800 nm for at least 25 s (Figure 6B; Supplemental Experimental Procedures). Under the selected distance threshold and time threshold, we estimated that >80% of the detected interacting lysosome-endosome pairs had a spatial overlap of their fluorescence signals during most (>80%) of the time that they stayed within the threshold distance (Figures S6B–S6F). Using our computational method, we counted interacting lysosome-endosome pairs in each cell and identified 26–117 pairs on average per cell in 5 min (Figure 6E). To examine the persistence of these candidate pairs, we calculated the time in which the pairs stayed within the distance threshold. We found that ~33% of the pairs stayed for >1 min (Figure 6F).

We then investigated the relations between the clusters of lysosomes and endosomes and the detected lysosome-endosome pairs. First, we identified clusters of lysosomes and clusters of endosomes, respectively (Figure 6C). Then, we checked the distribution of the interacting lysosome-endosome pairs within and outside the clusters (Figure 6D). We found that 23.5% of the interacting pairs resided within areas in which lysosome clusters overlapped with endosome clusters (Figure 6G); 50.5% of the interacting pairs resided in either a lysosomal cluster or an endosomal cluster. In total, 74% of the interacting pairs were associated with at least one cluster. In comparison, 26.0% of the interacting pairs were not within any clusters. Furthermore, we found that within 5 min, 12.7% ± 1.34% (mean ± SEM; n = 10 cells) of lysosomes inside clusters formed pairs with endosomes, while only 6.5% ± 0.97% (mean ± SEM; n = 10 cells) of lysosomes outside clusters formed pairs with endosomes, indicating that pairs were preferentially formed by lysosomes inside clusters (one-tailed t test; p = 0.0009). To further understand the behavior of the computationally detected interacting lysosome-endosome pairs, we studied their activities visually. As an example, we found that a pair stayed together for 566 s to complete their fusion (Figures 7A and 7B), which is consistent with the duration of fusion events reported in a previous study (Bright et al., 2005). Their fusion was confirmed based on their content exchange, as indicated by the fluorescence signals (Figures 7A and 7B).

Thus far, we have shown that clustering of lysosomes and endosomes are correlated with their significantly increased interactions. Given that lysosomes fuse with late endosomes, the clustering may be a secondary effect of the fusion, or, alternatively, the clustering promotes interactions such as fusion between lysosomes and endosomes. To differentiate between these two possibilities, we blocked the fusion of lysosomes with late endosomes using two strategies. First, we blocked the fusion by knocking down the hVps39 subunit of the HOPS complex (Supplemental Experimental Procedures), which has been shown to mediate the interactions between lysosomes and late endosomes (Pols et al., 2013; Wartosch et al., 2015). Second, we treated the cells with 1,2-bis(2-aminophenoxy) ethane-*N,N,N′,N′*-tetraacetic acid tetrakis(acetoxymethyl ester) (BAPTA-AM) (Figure S7A), a calcium chelator that has been shown to inhibit the delivery of endocytosed lipid cargo into lysosomes via the fusion of late endosome and lysosomes (Miedel

Figure 5. Formation of Lysosomal Clusters Is Associated with Local Increases in ER Spatial Density but Does Not Depend on Spatial Exclusion by Mitochondria

(A) Lysosomes remain tethered to the ER network. Left: a selected frame from a time-lapse video of a COS-7 cell in which ER and lysosomes were labeled. Right: zoomed-in views of selected frames of lysosomes in the rectangles. 1’: a lysosome undergoing directed movement. 2’: a lysosome undergoing constrained diffusion. 3’: a lysosome undergoing directed movement at the tip of a growing ER tubule. Scale bars, 5 μm (left), 1 μm (right).

(B) MSD analysis of the lysosome in panel 1’ of (A).

(C) MSD analysis of the lysosome in panel 2’ of (A).

(D) MSD analysis of a lysosome undergoing free diffusion (image not shown).

(E) Comparing ER spatial densities in clustered regions versus non-clustered regions. Segmented ER shown in white and background in gray. Lysosomes in clusters (red dots).Lysosomes not in any cluster (brown dots). Selected clusters for analysis (green contours). Randomly selected non-cluster regions with the same shape as a cluster (blue dash contours). Scale bar, 10 μm.

(F) Comparison of ER densities in cluster regions versus non-cluster regions. Cluster regions: 47.5% ± 7.6% (mean ± SD; n = 31 regions from 3 cells); non-cluster regions: 36.9% ± 9.0% (mean ± SD; n = 116 regions from 3 cells); $p = 1.2 \times 10^{-8}$. Error bars indicate SD.

(G–I) Selected frames at 0s (G), 28.5s (H), and 60.4s (I), from a time-lapse video of a COS-7 cell in which mitochondria and lysosomes were labeled. Scale bar, 10 μm.

(J–L) Lysosomal clusters and their spatial relations with mitochondria (shown in grayscale) 0s (J), 28.5s (K), and 60.4s (L). Lysosomes in clusters (red dots). Lysosomes not in any cluster (blue dots). Lysosome cluster boundaries (green dashed contours). Scale bar, 10 μm.

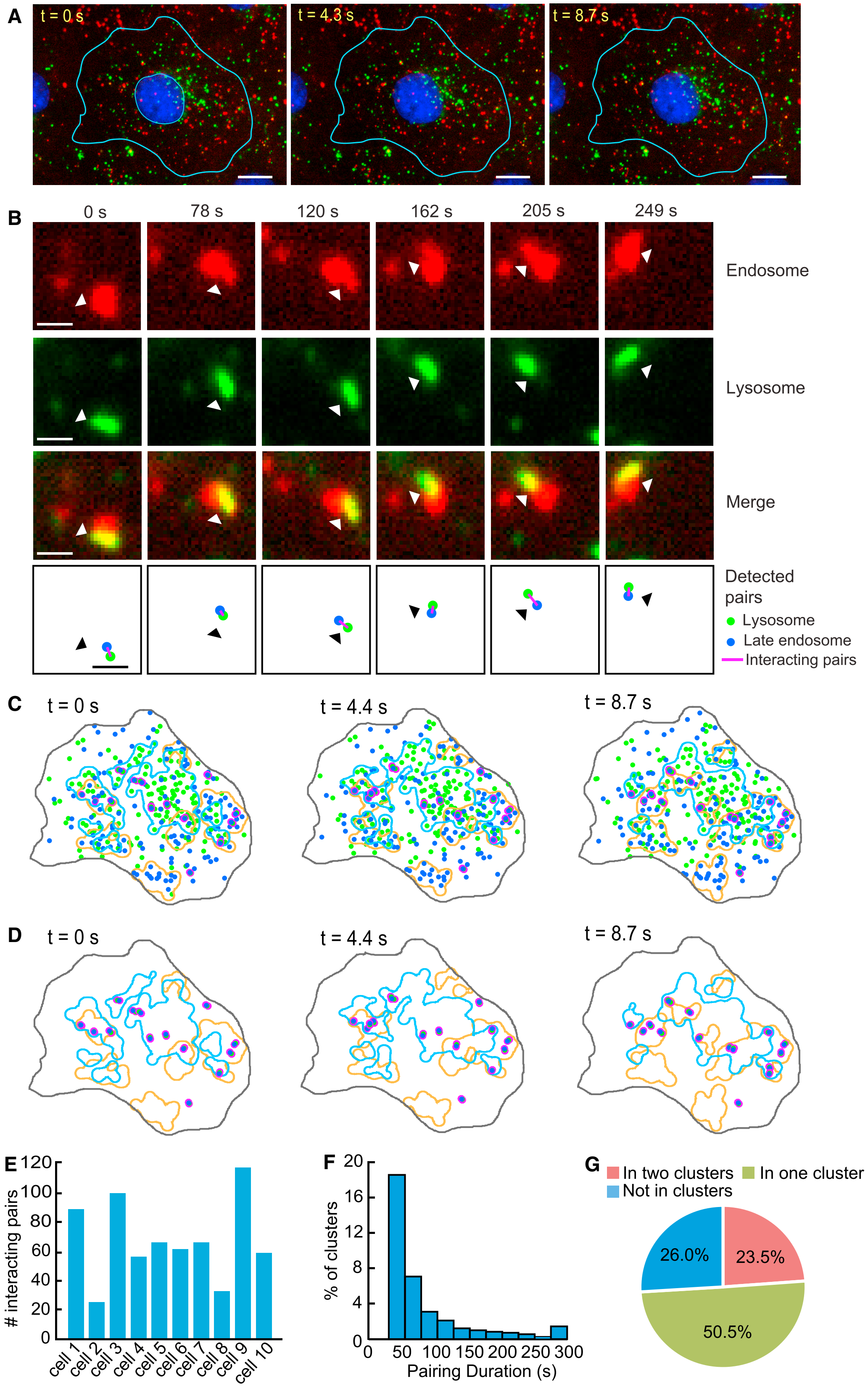

(legend on next page)

et al., 2008). In both cases, we found no change in either the average number of lysosomes or area per cluster in U2OS cells (Figures S7B–S7E). Taken together, these results indicate that the clustering of lysosomes is not merely a secondary effect of their fusion with late endosomes. We therefore conclude that the clustering of lysosomes significantly increases their interactions with endosomes.

DISCUSSION

The clustering of lysosomes in the perinuclear region has been noted from early studies of lysosomal motility and positioning (e.g., Matteoni and Kreis, 1987). However, the predominant view remains that individual lysosomes act independently and interact with partner organelles in an entirely random fashion. In the present study, we challenge this view. By combining high-resolution image analysis with spatial statistical analysis, we have found patterns in the collective behavior of lysosomes. Specifically, we find that despite their extensive long-distance movement, lysosomes maintain non-random, stable, yet distinct spatial distributions at the whole-cell scale (Figures 1C–1H and S2A–S2C). Furthermore, we find that by forming dynamic clusters throughout the intracellular space, individual lysosomes work together to increase their spatial density locally and to promote their interactions with endosomes (Figures 4A–4C, 6C, and 6D). Lysosomes likely bear similarities to other intracellular organelles such as endosomes and peroxisomes in their spatial organization because of their commonalities as compartments of the endomembrane system (Dacks et al., 2009; Diekmann and Pereira-Leal, 2013) and their extensive interactions (Bonifacino and Neefjes, 2017). Our findings that lysosomes maintain stable spatial distributions and form dynamic clusters create potentially fundamental concepts in lysosomal biology specifically and in organelle biology in general, and they provide insights into how organelle interactions are mediated and regulated at the whole-cell scale.

Functional Implications and Underlying Mechanisms of Stable yet Distinct Spatial Distributions of Lysosomes

Because of the crucial role lysosomes play in many important cellular processes, homeostasis of their functions is essential to cell homeostasis. We now know that at least some functions of lysosomes depend on their positioning (Johnson et al., 2016; Korolchuk et al., 2011). Because lysosomes maintain a dynamically stable spatial distribution at the whole-cell scale, homeostasis of their functions does not depend on fixed positions of individual lysosomes.

Our single-particle tracking reveals that lysosomes in a single cell form different subpopulations (Figures 3B and 3C). The subpopulation undergoing directed movement is maintained primarily by microtubule-based active transport. However, the subpopulation undergoing constrained diffusion is maintained only partially by the actin cytoskeleton (Figure 3C). The ER network also plays important roles in confining the movement of lysosomes (Figures 5A–5D). Overall, our analysis identifies at least three mechanisms that jointly mediate the stable spatial distribution of lysosomes at the whole-cell scale. The first mechanism is the balance between the subpopulation undergoing directed movement and the subpopulation undergoing constrained diffusion, which is essential to maintain a stable composition of the lysosomal population. The second mechanism is the balance between microtubule-based transport in the centrifugal direction and the centripetal direction, which is essential to maintain the overall positioning of lysosomes relative to one another and to the nucleus. The third mechanism is homeostasis in the biogenesis of lysosomes, which is essential to maintain the level of crowding between lysosomes (Figures 3H–3J). Additional mechanisms, especially upstream regulatory mechanisms, almost certainly are involved in maintaining the stable spatial distribution of lysosomes.

Roles of Organelle Interactions in Mediating Lysosomal Clustering

Recent studies such as that of Valm et al. (2017) revealed extensive interactions between lysosomes and other intracellular organelles. In particular, the ER network and mitochondria together account for the majority of the intracellular space excluding cytoplasm. In liver cells, for example, they account for ~80% of the intracellular space excluding cytoplasm (Alberts et al., 2014). In the present study, we find that the ER network not only confines lysosomal movement (Figures 5A–5D) but also may play a direct role in mediating lysosomal clustering (Figures 5E and 5F). Alternatively, spatial exclusion or restriction by mitochondria is not required for lysosomal clustering, even though it may contribute to the clustering (Figures 5G–5I and 5H–5J).

Functional Implications of Lysosomal Clustering

Using spatial statistical analysis techniques, we find that lysosomes form dynamic clusters not just in the perinuclear region but throughout the intracellular space (Figure 4C). We directly show that the clustering of lysosomes promotes their interactions with late endosomes (Figures 6C and 6D). A key benefit of the dynamic clustering of lysosomes is that it allows tuning

Figure 6. Clustering of Lysosomes Increases Their Interaction with Late Endosomes

(A) Selected frames from a time-lapse video of a COS-7 cell in which lysosomes (green) and late endosomes (red) were labeled. Scale bars, 15 μm.

(B) An example of a computationally detected interacting lysosome-endosome pair that remained together for >4 min. Top three rows: the actual fluorescence signals. Bottom row: computational detection result. Scale bars, 1 μm.

(C) Clusters of late endosomes and lysosomes detected from the video in (A). Interacting lysosome-endosome pairs (magenta). Lysosome (green). Late endosome (blue). Lysosome cluster boundaries (light blue lines). Endosome cluster boundaries (orange lines).

(D) Same as (E) but showing only the clusters and detected lysosome-endosome pairs.

(E) Number of detected interacting lysosome-endosome pairs in 10 cells within 5 min: 89, 26, 101, 54, 64, 61, 63, 32, 117, and 58.

(F) Histogram of the duration of the detected interacting pairs staying together.

(G) Relation between the location of interacting pairs and the clusters of endosomes and lysosomes.

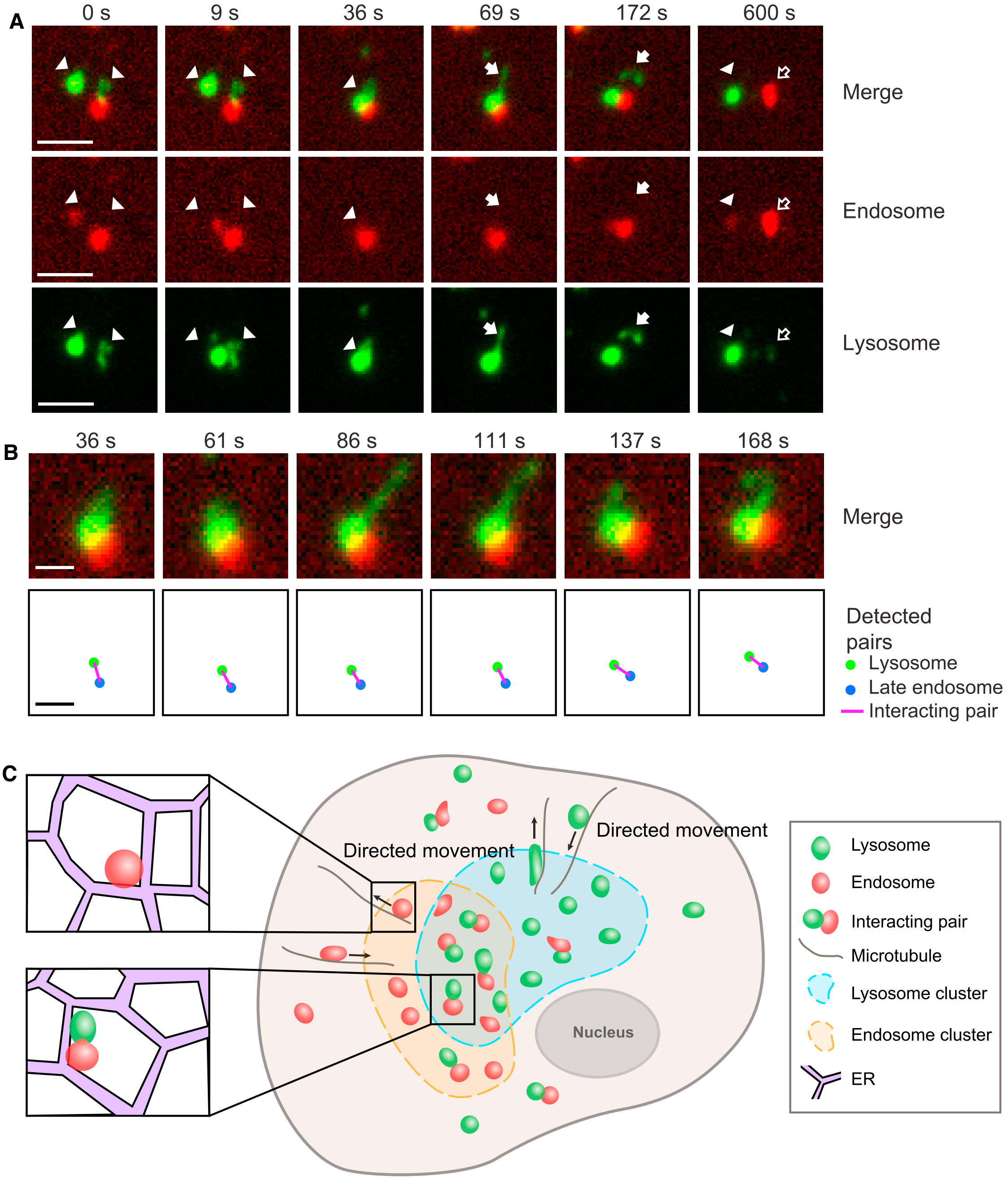

Figure 7. Tracking of Fusion between Lysosomes and Endosomes and a Model of Lysosomal Clustering

(A) An example of lysosome-endosome fusion in a COS-7 cell. At 0–9 s, two lysosomes (arrowheads) moved close to an endosome. At 36 s, the three organelles overlapped with one another in their fluorescence signals, presumably undergoing fusion or partial content exchange. This was followed by the formation of a new lysosome at 69–157 s, indicated by arrows. At 600 s, separation and content exchange were evident, given that the lysosome content (green fluorescence) was present in the endosome (hollow arrows) and vice versa. Lysosome (arrowheads). A newly formed lysosome (solid arrows). An endosome that gained lysosomal content (hollow arrows). Scale bar, 2.5 μm.

(B) Computational detection of lysosome-endosome interaction in the example shown in (A). (Upper row) The actual lysosome-endosome pair. (Bottom row) Computational detection results. Frame rate during imaging: 4.2 s per frame. Scale bars, 1 μm.

(C) Our active transport-mediated clustering model.

of the interaction of lysosomes with partner organelles locally throughout the intracellular space. By increasing the spatial density of lysosomes locally, the formation of clusters increases the likelihood of their collisions and interaction with partner organelles such as endosomes. More importantly, dynamic turnover of the clusters makes it possible to switch on or off such an effect. We speculate that dynamic clustering is a general mechanism for promoting and regulating organelle interactions.

Another key benefit of the dynamic clustering of lysosomes is that it facilitates the maintenance of lysosomal homeostasis. Lysosomes contain high levels of digestive enzymes (Luzio et al., 2007). Rupture of the lysosomal membrane under oxidative stress releases the enzymes into the cytoplasm and is known to trigger apoptosis under many conditions (Colletti et al., 2012; Sun et al., 2010). Therefore, to promote interactions of lysosomes with partner organelles through global crowding via a non-specific increase in their total number is not preferable, not only because this strategy lacks spatial specificity but also because it is detrimental to cell physiology. Dynamic clustering of lysosomes promotes their interactions with partner organelles without the need to increase their total numbers and thus facilitates the maintenance of lysosomal homeostasis.

A Model of Lysosomal Clustering

We propose an active transport-mediated clustering model (Figure 7C). Specifically, we propose that the formation and dispersion of lysosomal clusters are controlled by controlling the active transport of lysosomes, which are confined by the ER network. By increasing its spatial density locally, the ER network also directly contributes to the clustering of lysosomes.

EXPERIMENTAL PROCEDURES

Cell Lines

COS-7 cells were maintained in DMEM supplemented with 10% fetal bovine serum. BS-C-1 cells were maintained in Eagle's Minimum Essential Medium (EMEM) supplemented with 10% fetal bovine serum. U2OS cells were maintained in McCoy's 5A Medium (Thermo Fisher Scientific) supplemented with 10% fetal bovine serum. Cells, culture media, and serum were purchased from the American Type Culture Collection.

Fluorescence Microscopy

Imaging was performed on a Nikon Eclipse Ti-E inverted microscope with a CoolSNAP HQ2 camera (Photometric) and a 100×/1.40 numerical aperture (NA) or 60×/1.40 NA oil objective lens. The effective pixel sizes were 0.0645 μm at 100× and 0.107 μm at 60×, respectively. For experiments on ciliobrevin treatment, torin 1 treatment, mitochondria-lysosome interaction, and ER-lysosomes interaction, imaging was performed with an Andor Zyla complementary metal oxide semiconductor (CMOS) camera with a 60×/1.40 NA oil objective lens. The effective pixel size was 0.11 μm at 60×. During live imaging, cells were maintained in a Tokai HIT stage incubator at 37°C with 5% CO_2. LAMP1-mCherry for labeling late endosomes and lysosomes and dextran Alexa Fluor 594 for labeling endosomes were imaged using a tetramethylrhodamine (TRITC) filter set. Dextran Alexa Fluor 488 for labeling lysosomes was imaged using a fluorescein isothiocyanate (FITC) filter set. For each condition, at least six cells from two to three independent experiments were imaged.

Lysosomes in non-patterned cells were imaged at 4 frames per second. Lysosomes in patterned cells were imaged at 2.5 frames per second. One-hour videos of lysosomes in COS-7 cells were imaged at 25 s per frame. In latrunculin A, nocodazole, and ciliobrevin D treatment experiments, cells were imaged at 10 frames per second. In ER-lysosome colabeling experiments, cells were imaged at 2.0–2.5 s per frame. In mitochondria-lysosome colabeling experiments, cells were images at 1.5–1.7 s per frame. In endosome-lysosome interaction experiments, cells were imaged at 4.2–5 s/ per frame.

Statistical Methods

Unless specified otherwise, comparison of statistical distributions was performed using two-sample Kolmogorov-Smirnov tests, comparison of means was performed using two-sample t tests, and comparison of medians was performed using Wilcoxon rank sum tests.

DATA AND SOFTWARE AVAILABILITY

The custom software developed for this study is available in source code at https://github.com/ccdlcmu/LysosomeSpatialOrganization_code.

SUPPLEMENTAL INFORMATION

Supplemental Information includes Supplemental Experimental Procedures, seven figures, and seven videos and can be found with this article online at https://doi.org/10.1016/j.celrep.2018.05.079.

ACKNOWLEDGMENTS

Q.B. acknowledges a Bertucci Graduate Research Fellowship. K.K. acknowledges NIH grants NS096755 and NS094860. G.Y. acknowledges National Science Foundation CAREER grant DBI-1149494. The authors thank Sheiva Fakhraie and Liwia Andrzejcuk for their technical assistance.

AUTHOR CONTRIBUTIONS

G.Y., K.K., and Q.B. conceived and designed the project. Q.B. performed the experiments. G.Y., Q.B., and G.R. performed the data analysis. K.K. contributed to the experimental design and data analysis and provided some reagents. G.Y. and Q.B. wrote the manuscript with contributions from the other authors.

DECLARATION OF INTERESTS

The authors declare no competing interests.

Received: October 12, 2017
Revised: April 14, 2018
Accepted: May 23, 2018
Published: June 19, 2018

REFERENCES

Alberts, B., Johnson, A., Lewis, J., Morgan, D., Raff, M., Roberts, K., and Walter, P. (2014). Molecular Biology of the Cell, Sixth Edition (Garland Science).

Baddeley, A., Rubak, E., and Turner, R. (2016). Spatial Point Patterns: Methodology and Applications with R (Chapman & Hall/CRC).

Bandyopadhyay, D., Cyphersmith, A., Zapata, J.A., Kim, Y.J., and Payne, C.K. (2014). Lysosome transport as a function of lysosome diameter. PLoS One *9*, e86847.

Boland, M.V., and Murphy, R.F. (2001). A neural network classifier capable of recognizing the patterns of all major subcellular structures in fluorescence microscope images of HeLa cells. Bioinformatics *17*, 1213–1223.

Bonifacino, J.S., and Neefjes, J. (2017). Moving and positioning the endolysosomal system. Curr. Opin. Cell Biol. *47*, 1–8.

Bright, N.A., Gratian, M.J., and Luzio, J.P. (2005). Endocytic delivery to lysosomes mediated by concurrent fusion and kissing events in living cells. Curr. Biol. *15*, 360–365.

Caviston, J.P., Zajac, A.L., Tokito, M., and Holzbaur, E.L.F. (2011). Huntingtin coordinates the dynein-mediated dynamic positioning of endosomes and lysosomes. Mol. Biol. Cell *22*, 478–492.

Colletti, G.A., Miedel, M.T., Quinn, J., Andharia, N., Weisz, O.A., and Kiselyov, K. (2012). Loss of lysosomal ion channel transient receptor potential channel mucolipin-1 (TRPML1) leads to cathepsin B-dependent apoptosis. J. Biol. Chem. *287*, 8082–8091.

Dacks, J.B., Peden, A.A., and Field, M.C. (2009). Evolution of specificity in the eukaryotic endomembrane system. Int. J. Biochem. Cell Biol. *41*, 330–340.

Diekmann, Y., and Pereira-Leal, J.B. (2013). Evolution of intracellular compartmentalization. Biochem. J. *449*, 319–331.

Diggle, P.J. (2014). Statistical Analysis of Spatial and Spatiotemporal Point Patterns, Third Edition (CRC Press).

Encarnação, M., Espada, L., Escrevente, C., Mateus, D., Ramalho, J., Michelet, X., Santarino, I., Hsu, V.W., Brenner, M.B., Barral, D.C., and Vieira, O.V. (2016). A Rab3a-dependent complex essential for lysosome positioning and plasma membrane repair. J. Cell Biol. *213*, 631–640.

Eskelinen, E.-L., and Saftig, P. (2009). Autophagy: a lysosomal degradation pathway with a central role in health and disease. Biochim. Biophys. Acta *1793*, 664–673.

Ester, M., Kriegel, H.-P., Sander, J., and Xu, X. (1996). A density-based algorithm for discovering clusters in large spatial databases with noise. In Proceedings of the 2nd International Conference on Knowledge Discovery and Data Mining, E. Simoudis, J. Han, and U. Fayyad, eds. (AAAI Press), pp. 226–231.

Firestone, A.J., Weinger, J.S., Maldonado, M., Barlan, K., Langston, L.D., O'Donnell, M., Gelfand, V.I., Kapoor, T.M., and Chen, J.K. (2012). Small-molecule inhibitors of the AAA+ ATPase motor cytoplasmic dynein. Nature *484*, 125–129.

Friedman, J.R., Dibenedetto, J.R., West, M., Rowland, A.A., and Voeltz, G.K. (2013). Endoplasmic reticulum-endosome contact increases as endosomes traffic and mature. Mol. Biol. Cell *24*, 1030–1040.

Glory, E., and Murphy, R.F. (2007). Automated subcellular location determination and high-throughput microscopy. Dev. Cell *12*, 7–16.

Gottschling, D.E., and Nyström, T. (2017). The upsides and downsides of organelle interconnectivity. Cell *169*, 24–34.

Illian, J., Penttinen, A., Stoyan, H., and Stoyan, D. (2008). Statistical Analysis and Modeling of Spatial Point Patterns (Wiley).

Johnson, G.R., Li, J., Shariff, A., Rohde, G.K., and Murphy, R.F. (2015). Automated learning of subcellular variation among punctate protein patterns and a generative model of their relation to microtubules. PLoS Comput. Biol. *11*, e1004614.

Johnson, D.E., Ostrowski, P., Jaumouillé, V., and Grinstein, S. (2016). The position of lysosomes within the cell determines their luminal pH. J. Cell Biol. *212*, 677–692.

Jongsma, M.L., Berlin, I., Wijdeven, R.H., Janssen, L., Janssen, G.M., Garstka, M.A., Janssen, H., Mensink, M., van Veelen, P.A., Spaapen, R.M., and Neefjes, J. (2016). An ER-associated pathway defines endosomal architecture for controlled cargo transport. Cell *166*, 152–166.

Korolchuk, V.I., Saiki, S., Lichtenberg, M., Siddiqi, F.H., Roberts, E.A., Imarisio, S., Jahreiss, L., Sarkar, S., Futter, M., Menzies, F.M., et al. (2011). Lysosomal positioning coordinates cellular nutrient responses. Nat. Cell Biol. *13*, 453–460.

Li, X., Rydzewski, N., Hider, A., Zhang, X., Yang, J., Wang, W., Gao, Q., Cheng, X., and Xu, H. (2016). A molecular mechanism to regulate lysosome motility for lysosome positioning and tubulation. Nat. Cell Biol. *18*, 404–417.

Lim, C.-Y., and Zoncu, R. (2016). The lysosome as a command-and-control center for cellular metabolism. J. Cell Biol. *214*, 653–664.

Luby-Phelps, K., Lanni, F., and Taylor, D.L. (1988). The submicroscopic properties of cytoplasm as a determinant of cellular function. Annu. Rev. Biophys. Biophys. Chem. *17*, 369–396.

Luzio, J.P., Pryor, P.R., and Bright, N.A. (2007). Lysosomes: fusion and function. Nat. Rev. Mol. Cell Biol. *8*, 622–632.

Martens, S., and McMahon, H.T. (2008). Mechanisms of membrane fusion: disparate players and common principles. Nat. Rev. Mol. Cell Biol. *9*, 543–556.

Matteoni, R., and Kreis, T.E. (1987). Translocation and clustering of endosomes and lysosomes depends on microtubules. J. Cell Biol. *105*, 1253–1265.

Miedel, M.T., Rbaibi, Y., Guerriero, C.J., Colletti, G., Weixel, K.M., Weisz, O.A., and Kiselyov, K. (2008). Membrane traffic and turnover in TRP-ML1-deficient cells: a revised model for mucolipidosis type IV pathogenesis. J. Exp. Med. *205*, 1477–1490.

Pols, M.S., ten Brink, C., Gosavi, P., Oorschot, V., and Klumperman, J. (2013). The HOPS proteins hVps41 and hVps39 are required for homotypic and heterotypic late endosome fusion. Traffic *14*, 219–232.

Prinz, W.A. (2014). Bridging the gap: membrane contact sites in signaling, metabolism, and organelle dynamics. J. Cell Biol. *205*, 759–769.

Pu, J., Schindler, C., Jia, R., Jarnik, M., Backlund, P., and Bonifacino, J.S. (2015). BORC, a multisubunit complex that regulates lysosome positioning. Dev. Cell *33*, 176–188.

Pu, J., Guardia, C.M., Keren-Kaplan, T., and Bonifacino, J.S. (2016). Mechanisms and functions of lysosome positioning. J. Cell Sci. *129*, 4329–4339.

Qian, H., Sheetz, M.P., and Elson, E.L. (1991). Single particle tracking. Analysis of diffusion and flow in two-dimensional systems. Biophys. J. *60*, 910–921.

Raiborg, C., Wenzel, E.M., Pedersen, N.M., Olsvik, H., Schink, K.O., Schultz, S.W., Vietri, M., Nisi, V., Bucci, C., Brech, A., et al. (2015). Repeated ER-endosome contacts promote endosome translocation and neurite outgrowth. Nature *520*, 234–238.

Sardiello, M., Palmieri, M., di Ronza, A., Medina, D.L., Valenza, M., Gennarino, V.A., Di Malta, C., Donaudy, F., Embrione, V., Polishchuk, R.S., et al. (2009). A gene network regulating lysosomal biogenesis and function. Science *325*, 473–477.

Sarkar, S., Davies, J.E., Huang, Z., Tunnacliffe, A., and Rubinsztein, D.C. (2007). Trehalose, a novel mTOR-independent autophagy enhancer, accelerates the clearance of mutant huntingtin and α-synuclein. J. Biol. Chem. *282*, 5641–5652.

Saxton, M.J. (1997). Single-particle tracking: the distribution of diffusion coefficients. Biophys. J. *72*, 1744–1753.

Settembre, C., Di Malta, C., Polito, V.A., Garcia Arencibia, M., Vetrini, F., Erdin, S., Erdin, S.U., Huynh, T., Medina, D., Colella, P., et al. (2011). TFEB links autophagy to lysosomal biogenesis. Science *332*, 1429–1433.

Settembre, C., Fraldi, A., Medina, D.L., and Ballabio, A. (2013). Signals from the lysosome: a control centre for cellular clearance and energy metabolism. Nat. Rev. Mol. Cell Biol. *14*, 283–296.

Sun, L., Zhao, Y., Li, X., Yuan, H., Cheng, A., and Lou, H. (2010). A lysosomal-mitochondrial death pathway is induced by solamargine in human K562 leukemia cells. Toxicol. In Vitro *24*, 1504–1511.

Thoreen, C.C., Kang, S.A., Chang, J.W., Liu, Q., Zhang, J., Gao, Y., Reichling, L.J., Sim, T., Sabatini, D.M., and Gray, N.S. (2009). An ATP-competitive mammalian target of rapamycin inhibitor reveals rapamycin-resistant functions of mTORC1. J. Biol. Chem. *284*, 8023–8032.

Valm, A.M., Cohen, S., Legant, W.R., Melunis, J., Hershberg, U., Wait, E., Cohen, A.R., Davidson, M.W., Betzig, E., and Lippincott-Schwartz, J. (2017). Applying systems-level spectral imaging and analysis to reveal the organelle interactome. Nature *546*, 162–167.

Wartosch, L., Günesdogan, U., Graham, S.C., and Luzio, J.P. (2015). Recruitment of VPS33A to HOPS by VPS16 is required for lysosome fusion with endosomes and autophagosomes. Traffic *16*, 727–742.

Yu, L., McPhee, C.K., Zheng, L., Mardones, G.A., Rong, Y., Peng, J., Mi, N., Zhao, Y., Liu, Z., Wan, F., et al. (2010). Termination of autophagy and reformation of lysosomes regulated by mTOR. Nature *465*, 942–946.

Cell Reports, Volume *23*

Supplemental Information

Whole-Cell Scale Dynamic Organization of Lysosomes Revealed by Spatial Statistical Analysis

Qinle Ba, Guruprasad Raghavan, Kirill Kiselyov, and Ge Yang

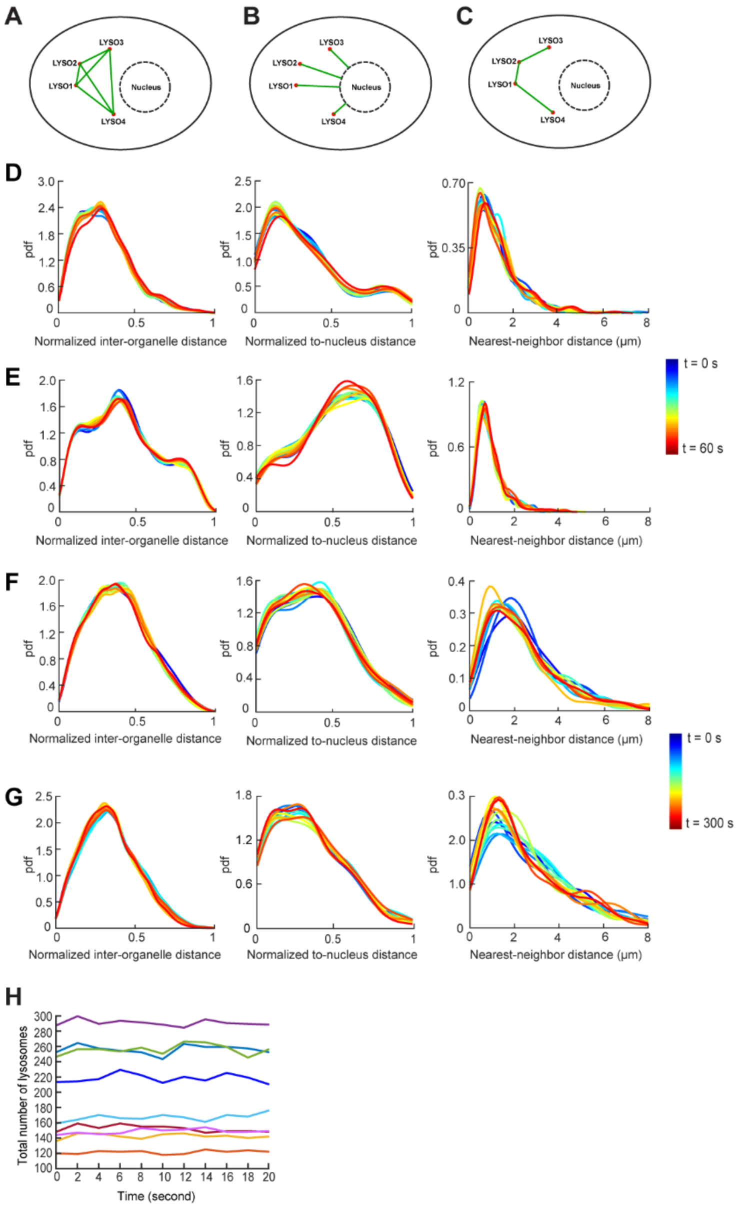

Figure S1. Related to Figure 1. Spatial distributions and total numbers of lysosomes remain stable over time in single cells. (A) A cartoon illustration of inter-organelle distances. (B) A cartoon illustration of to-nucleus distances. (C) A cartoon illustration of nearest-neighbor distances. (D) and (E): Distributions of the three distances of lysosomes from two BS-C-1 cells. Each distribution was plotted every 5 seconds over 60 seconds, hence 13 plots. The temporal variations were quantified using Sorensen dissimilarity scores. A total of 13 distributions were compared pairwise, hence $C_{13}^{2} = 78$ pairs. pdf: probability density function. (D) Temporal variations (mean ± STD; n = 78): normalized inter-organelle distance distribution, 1.77% ± 0.64%; normalized to-nucleus distance distribution, 2.53% ± 0.72%; nearest-neighbor distance distribution, 8.64% ± 2.65%. (E) Temporal variations (mean ± STD; n = 78): normalized inter-organelle distance distribution, 1.87% ± 0.61%; normalized to-nucleus distance distribution: 2.60% ± 1.04%; nearest-neighbor distance distribution, 6.07% ± 1.51%. (F) and (G): three distance distributions of lysosomes from two COS-7 cells. Each distribution was plotted every 25 seconds over 300 seconds, hence 13 plots. (F) Temporal variations (mean ± STD; n = 78): normalized inter-organelle distance distribution, 1.53% ± 1.43%; normalized to-nucleus distance distribution, 2.04% ± 1.75%; nearest-neighbor distance distribution, 5.19% ± 4.47%. (G) Temporal variations (mean ± STD; n = 78): normalized inter-organelle distance distribution, 1.71% ± 1.66%; normalized to-nucleus distance distribution, 1.94% ± 1.63%; nearest-neighbor distance distribution, 5.55% ± 4.49%. (H) Total numbers of lysosomes in COS-7 cells during 20 seconds of imaging, plotted every 2 seconds for each cell, n = 9 cells. Frame rate: 10 frames per second. Total numbers of lysosomes in each cell (mean ± STD): 122 ± 2, 142 ± 3, 149 ± 3, 152 ± 4, 167 ± 5, 218 ± 6, 255 ± 7, 256 ± 6, 290 ± 4.

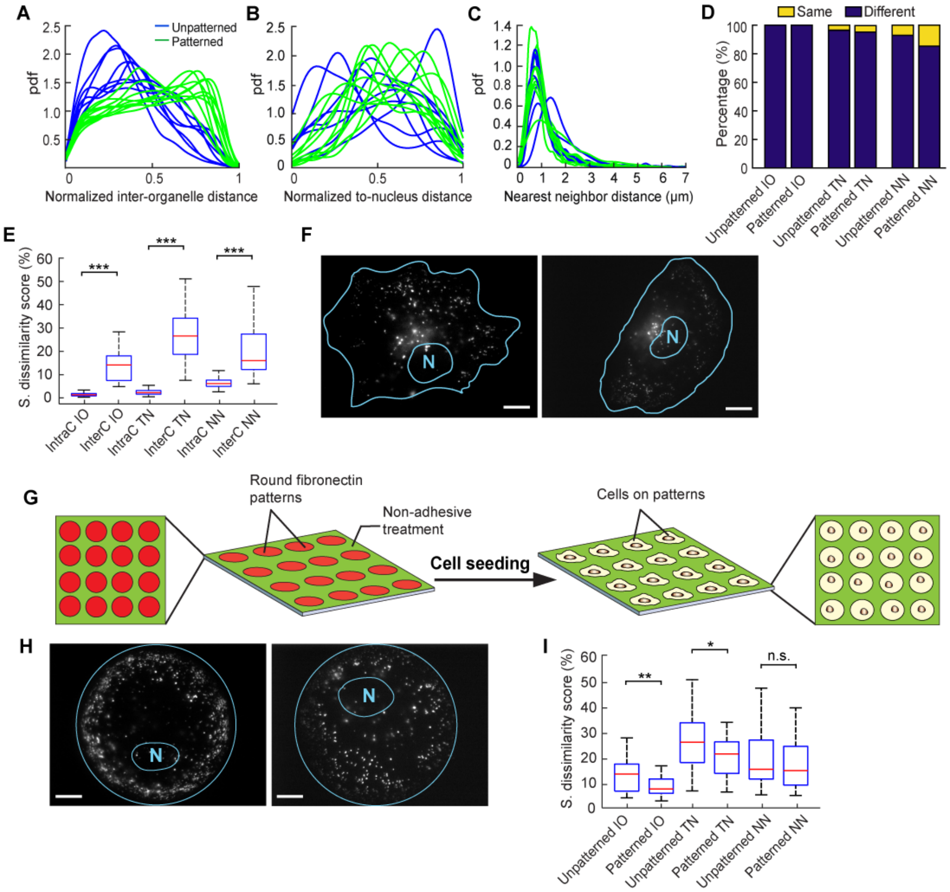

Figure S2. Related to Figure 1. Distinct lysosomal distributions in singles cells are not merely a secondary effect of their distinct shapes. (A-C) Comparison of three distance distributions in non-patterned cells (blue lines; n = 8) and patterned cells (green lines; n = 10). (D) Results of pairwise comparison of the three distance distributions among non-patterned (total = 28 comparisons; left columns) and patterned cells (total = 45 comparisons; right columns) using two-sample Kolmogorov-Smirnov tests. Cutoff p-value for statistical significance: 0.05. IO: normalized inter-organelle distance distribution; TN: normalized to-nucleus distance distribution; NN: nearest-neighbor distance distribution. Percentage of comparison showing significant differences: IO: 100% (non-patterned) and 100% (patterned); TN: 96.4% (non-patterned) and 95.6% (patterned); NN: 92.9% (non-patterned) and 84.4% (patterned). (E) Comparison of intracellular (intraC) variations of the distance distributions within single cells versus intercellular (interC) variations of the distributions among different cells using Wilcoxon rank sum tests. All variations represented in Sorensen dissimilarity scores. IO: intracellular: 1.64% ± 1.38% (mean ± STD; n = 624 scores; data pooled from 8 cells with 78 scores per cell), intercellular: 14.42% ± 7.27% (mean ± STD; n = 28 scores from 8 cells), p-value: 1.3×10^{-18}; TN: intracellular: 2.67% ± 1.80%, intercellular: 27.89% ± 12.83%, p-value: 4.5×10^{-19}; NN: intracellular: 6.46% ± 2.14%, intercellular: 21.53% ± 13.42%, p-value: 1.2×10^{-15}. Notation for p values: *, $p < 0.05$; **, $p < 0.01$; ***, $p < 0.001$. (F) Examples of unpatterned cells with different shapes. Scale bars: 10 μm. (G) A cartoon illustrating the process of patterning shapes of cells by growing them on patterned fibronectin substrates. (H) Examples of patterned cells. Scale bars: 10 μm. (I) Comparison of intercellular variations of non-patterned cells versus patterned cells using one-tailed Wilcoxon rank sum tests. IO: non-patterned: 14.42% ± 7.27% (mean ± STD; n = 28 scores from 8 cells); patterned: 9.42% ± 3.99% (mean ± STD; n = 45 scores from 10 cells), p-value: 0.0037. TN: non-patterned: 27.89% ± 12.83%; patterned: 20.65% ± 7.63%, p-value: 0.016. NN: non-patterned: 21.53% ± 13.42%; patterned: 18.94% ± 10.50%, p-value: 0.59.

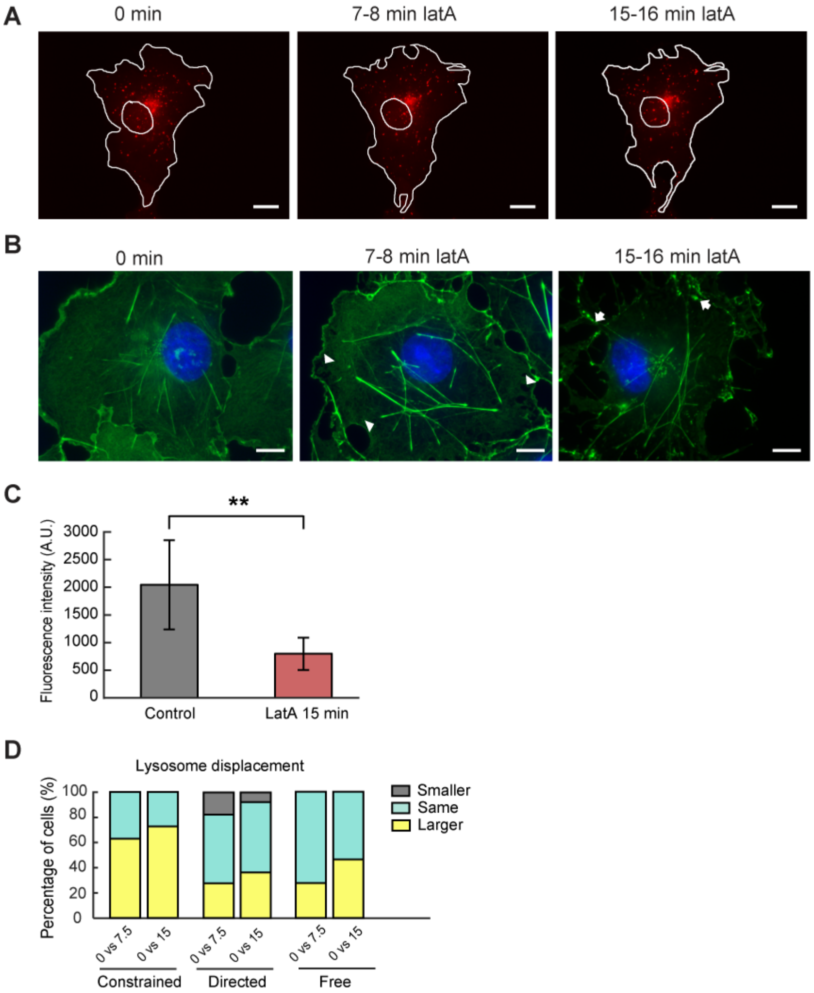

Figure S3. Related to Figure 3. Changes of actin network and lysosomal movement under latrunculin A treatment. (A) Shape changes of a COS-7 cell transfected with mCherry-Lamp1 at different time points before and after treatment of 0.8 μM of latrunculin A. Red, lysosomes. Scale bars: 15 μm. (B) COS-7 cells fixed and stained with phalloidin (Actin-stain 488) under control condition and after 7.5 min and 15 min of latA (0.8 μM) treatment. Arrow heads point to regions with reduced phalloidin fluorescence signals. Arrows point to actin patches. Scale bars, 10 μm. (C) Quantification of fluorescence intensity of actin in control and latA treated cells. A.U., arbitrary unit. Control: 2048 ± 807 (mean ± STD; n = 7 cells); latA 15 min: 799 ± 289 (mean ± STD; n = 7 cells). A one-tailed unpaired student-t test was performed; p-value, 0.0098. (D) Comparison of displacement of different lysosomal subpopulations within 5 seconds before and after latA treatment in single cells: before treatment (0 min) vs 7.5 min; before treatment (0 min) vs. 15 min. n = 11 cells. One-tailed unpaired student-t tests were performed with a cutoff significance level of 0.05. Constrained diffusion, 0 min vs 7.5 min: smaller, 0%; same 36.4%; larger: 63.6%; constrained, 0 min vs 15 min: smaller 0%; same 27.3%; larger 72.7%. Directed movement, 0 vs 7.5 min: smaller 18.2%; same 54.5%; larger 27.3%; directed, 0 vs 15 min: smaller 9.1%; same 54.5%; larger 36.4%. Free diffusion, 0 vs 7.5 min: smaller 0%; same 72.7%; larger 27.3%; free diffusion, 0 vs 15 min: smaller 0%; same 54.5%; larger 45.5%.

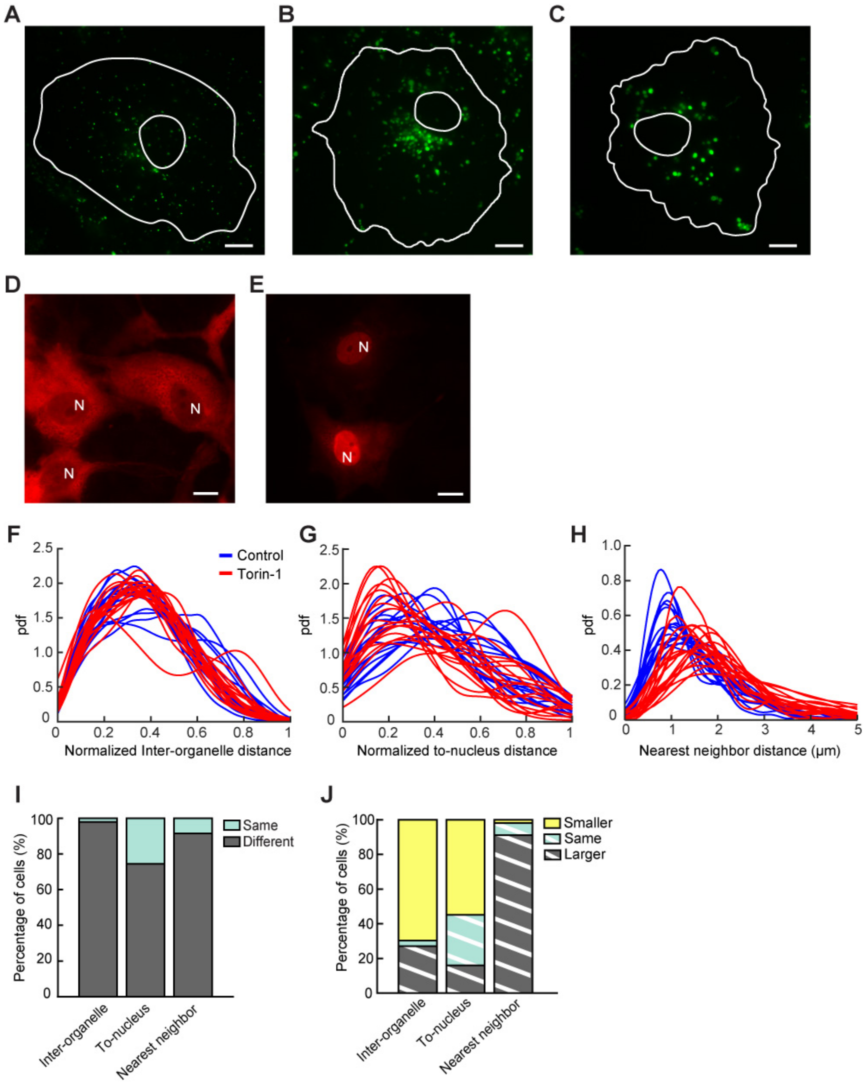

Figure S4. Related to Figure 3. Changes of lysosomal spatial distribution upon torin-1 treatment. (A-C) Changed distributions of lysosomes labeled with dextran Alexa-488 (green) in COS-7 cells under torin-1 treatment. A: Control (DMSO). (B) and (C): Two different cells treated with 2 μM torin-1 for 13.5 hours. Scale bars: 10 μm. (D-E) COS-7 cells transfected with TFEB-myc was stained with rabbit anti-myc antibody and mouse anti-rabbit Alexa 594 secondary antibody. (D) Control (DMSO). N, cell nucleus. (E) 2 μM torin-1 treated for 4 hours. (F-H) The three distance distributions in control cells (n = 15) versus torin-1 treated cells (13.5 hours, 18 cells). (I) Comparison of distributions in control cells versus cells treated with torin-1 using two sample Kolmogorov-Smirnov tests (n = 270 pairs). Inter-organelle (different, same): 99.3%, 0.7%; To-nucleus: 75.7%, 24.3%; Nearest-neighbor: 91.5%, 8.5%. (J) Comparison of median distances in control cells versus cells treated with torin-1 using one-tailed Wilcoxon rank sum tests (n = 270 pairs). Inter-organelle (smaller, same, larger): 69.6%, 3.4%, 27.0%; To-nucleus: 54.8%, 29.2%, 15.9%; Nearest-neighbor: 0.4%, 8.5%, 91.1%.

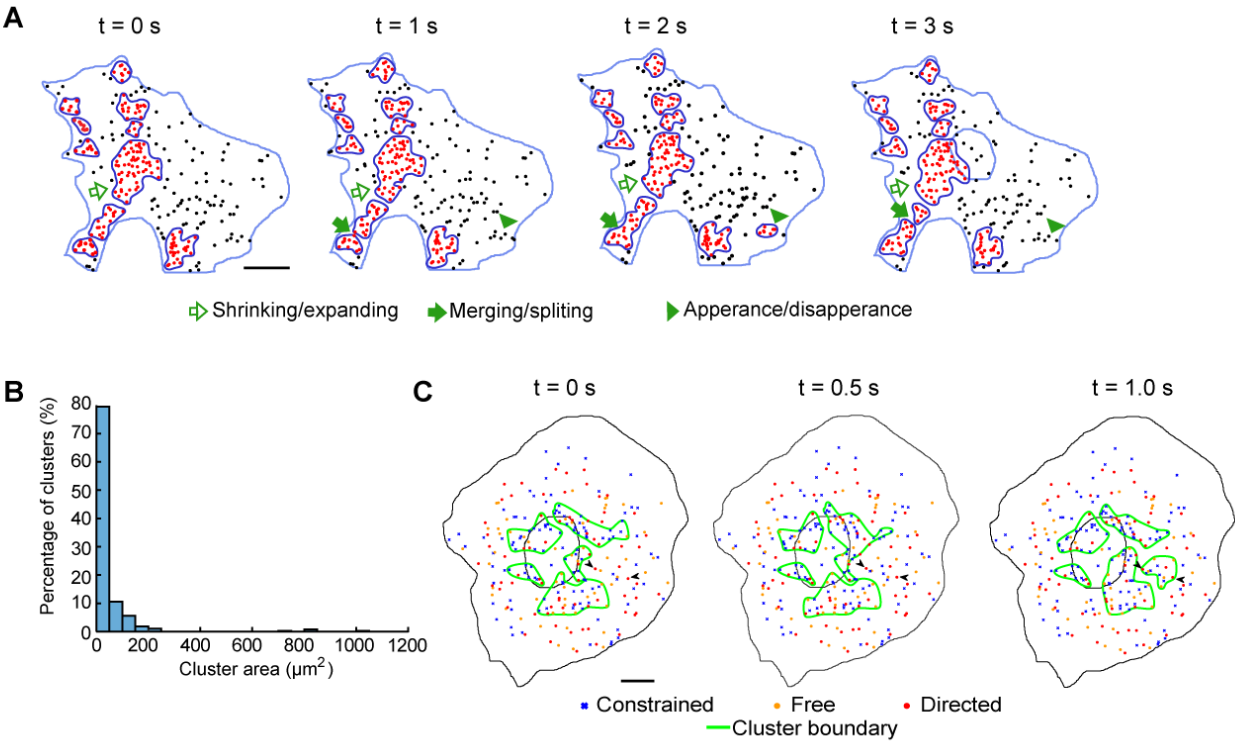

Figure S5. Related to Figure 4. Dynamic turnover and size distribution of lysosomal clusters. (A) Various dynamic turnover events of lysosomal clusters in a COS-7 cell. Scale bar, 15 μm. (B) Size distribution of lysosomal clusters in COS-7 cells. The average area of clusters was 47.2 ± 6.5 μm^2 (mean ± SEM; n = 376 clusters from 9 cells). (C) An example of formation of a cluster, which was mediated by two lysosomes undergoing directed movement (arrowheads) together with lysosomes undergoing constrained diffusion and free diffusion. The entire event was shown in video S4. For simplicity, only large clusters with more than 10 lysosomes were shown. Scale bar, 10 μm.

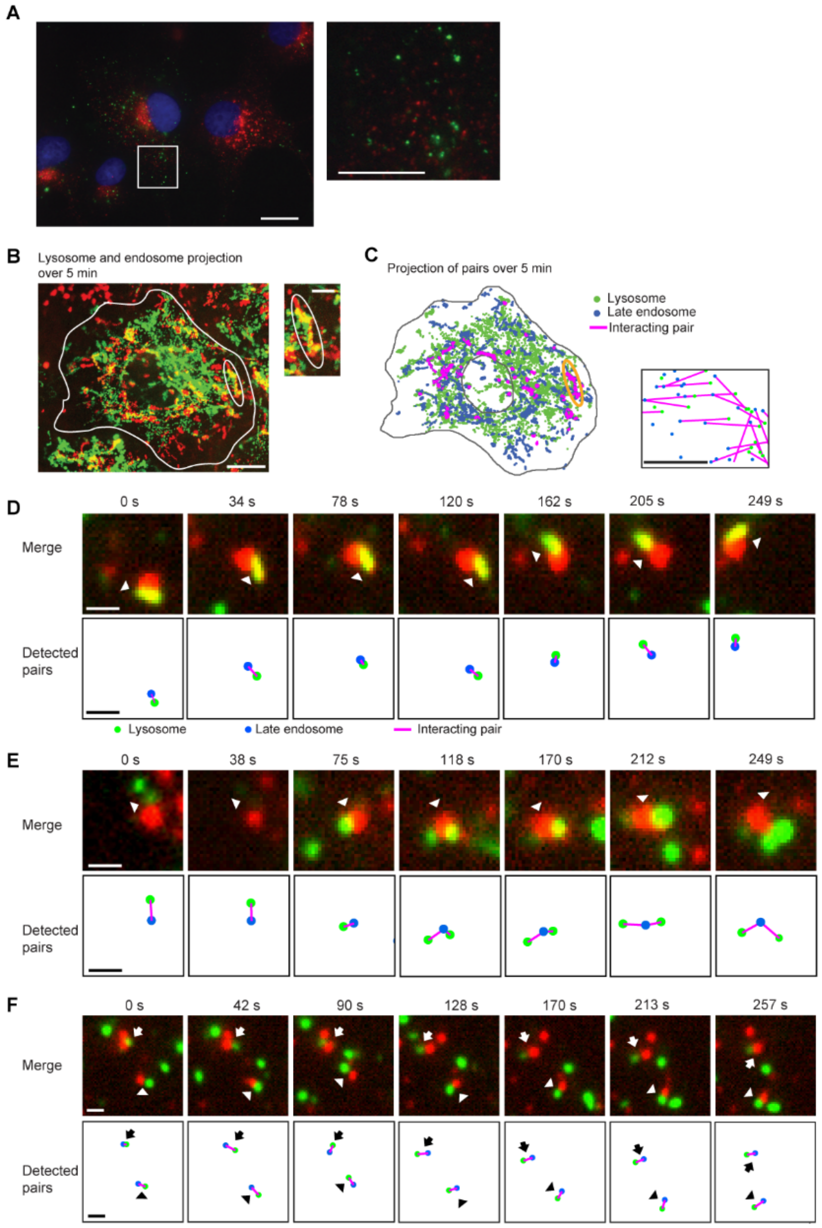

Figure S6. Related to Figure 6 & Figure 7. Fluorescent labeling and computational detection of lysosome-endosome pairs. (A) Validation of specific labeling of lysosomes as terminal endocytic compartments differentiated from late endosomes. Left panel: COS-7 cells labeled with dextran Alexa 488 for lysosome and immunostained for anti-Mannose-6-phosphate receptor (anti-M6PR). Lysosomes are defined as terminal endocytic compartments lacking M6PR (Griffiths et al., 1988; Luzio et al., 2007). They were labeled with a 3 hr pulse of dextran Alexa 488 followed by a 20 hour chase (Bright et al., 2005). Most lysosomes (green) did not colocalize with M6PR (red). Right panel: zoom-in view of the boxed area in the left panel. Blue, cell nucleus. Scale bars: left panel, 20 μm; right panel, 10 μm. (B) Left panel: maximum intensity projection of late endosomes (red) and lysosomes (green) of a 5-minute movie imaged at ~5 seconds per frame. Yellow signals indicate colocalized endosome-lysosome pairs. The circled region shows the trajectory of a computationally detected endosome-lysosome pair. Inset: zoomed in view of the circled region. Scale bars: left panel, 15 μm; inset, 5 μm. (C) Left panel: maximum intensity projection of late endosomes (blue) and lysosomes (green) and detected pairs (magenta), from the same 5-minute movie as in (B). Inset: zoomed-in view of detected pairs. Scale bar: inset, 500 nm. (D-F) Various examples of computationally detected interacting lysosome-endosome pairs (lower rows) and their actual fluorescence signals (upper rows). The pairs of organelles remained associated for at least 4 minutes. (D) An interacting lysosome-endosome pair. (E) An endosome initially interacted with one and then two lysosomes. (F) Two detected lysosome-endosome pairs close to each other. Scale bars: 1 μm.

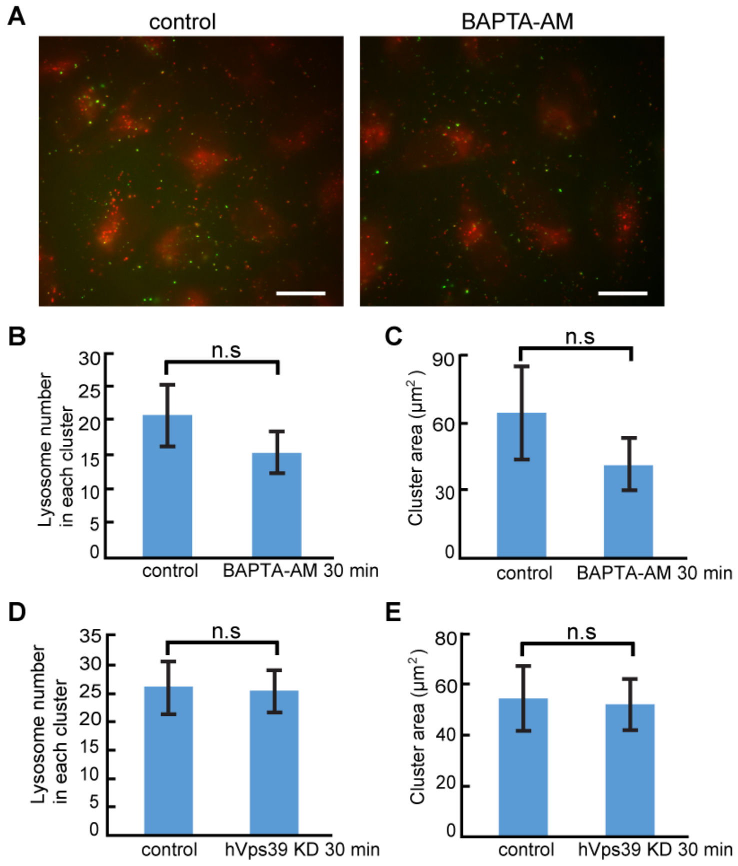

Figure S7. Related to Figure 6 & Figure 7. Clustering of lysosomes does not depend on fusion with late endosomes. (A-B) COS-7 cell labeled with dextran Alexa-488 for 15 min and chased for 30 min for endosomes (green), and co-labeled with Magic Red Cathepsin-B kit for lysosomes (red). (A) Control (DMSO). (B) 10 μM BAPTA-AM treated starting from chasing. Scale bars: 20 μm. (B-E) Error bars show standard deviation. All statistical comparisons were made using one-tailed unpaired student-t tests. (B) Comparison of the number of lysosomes in clusters under control and in BAPTA-AM treated cells (n = 12 cells). p-value: 0.3. (C) Comparison of lysosomal cluster areas under control and in BAPTA-AM treated cells (n = 12 cells). p-value: 0.4. (D) Comparison of the number of lysosomes in clusters under control (n = 12 cells) and in hVps39 knockdown cells (n = 12 cells). p-value: 0.5. (E) Comparison of lysosomal cluster areas under control (n = 12 cells) and in hVps39 knockdown cells (n = 12 cells). p-value: 0.5.

Supplemental Experimental Procedures

Fluorescence Labeling of Organelles

Lysosomes in COS-7 cells were labeled by transfecting 200-300 ng of LAMP1-mCherry. Transfection of COS-7 cells was performed using the Neon electroporation system (Invitrogen, Carlsbad, CA). Briefly, 2×10^5 cells were suspended in a 10 µl pipette tip and electroprated under a pulse voltage of 950 V, a pulse width of 30 ms, and a pulse number of 2. Following transfection, cells were seeded at 6.7×10^4 per 20 mm glass well in 35 mm dishes (MatTek, Ashland, MA) and incubated for 24-48 hours before imaging. Lysosomes in BS-C-1 cells were labeled as described in (Bright et al., 2005; Humphries et al., 2011; Kilpatrick et al., 2015). Briefly, cells were incubated with 0.5 mg/ml dextran Alexa 488, 10000 MW (Molecular Probes, Eugene, OR) for 3-4 hours followed by 16 hours of chasing. Late endosomes and lysosomes in COS-7 cells were co-labelled as described in (Bright et al., 2005; Bright et al., 2015). Briefly, cells were incubated with 0.5 mg/ml dextran Alexa 488 for 3 hours, followed by 20-27 hours of chasing to mark lysosomes. Then cells were incubated with 0.5 mg/ml dextran Alexa 594, 10000 MW (Molecular Probes, Eugene, OR) for 10 minutes followed by 10 minutes of chasing to mark endosomes before imaging. That the co-labeling scheme reliably differentiated late endosomes from lysosomes was validated as described in (Bright et al., 2005; Luzio et al., 2007) by immunostaining of Mannose-6 phosphate receptor (M6PR), a marker present in endosomes but not in lysosomes, using a monoclonal M6PR antibody (MA1-066; Thermo Fisher).

Drug Treatment

To depolymerize microtubules, COS-7 cells were treated with 2.5 µM nocodazole (Sigma-Aldrich, St. Louis, MO) and imaged before and 15 minutes and 30 minutes after treatment for the same cells. To inhibit cytoplasmic dynein, COS-7 cells were treated with 80 µM ciliobrevin D (Sigma-Aldrich, St. Louis, MO) and imaged before and 1 hour after treatment for the same cells. To depolymerize actin filaments, COS-7 cells were treated with 800 nM latrunculin A (Sigma-Aldrich, St. Louis, MO) and imaged before and 7-8 minutes and 15-16 minutes after treatment. To examine the effect of latrunculin A treatment on the actin cytoskeleton, cells were fixed and stained with fluorescent phalloidin (Actin-staining 488 fluorescent phalloidin; Cytoskeleton, Denver, CO) following instructions of the manufacturer. To upregulate lysosomal biogenesis and autophagy, cells were treated with 50 mM trehalose (Sigma-Aldrich, St. Louis, MO) as described in (Palmieri et al., 2017; Porter et al., 2013; Sarkar et al., 2007) and imaged after 12 hours of treatment, or treated with 2µM torin 1 (Tocris Bioscience, Bristol, United Kingdom) as described in (Martina et al., 2012; Thoreen et al., 2009) and imaged after 2 hours up to 14 hours. To verify activation of TFEB by torin-1 treatment (Martina et al., 2012; Thoreen et al., 2009), cells were transfected with TFEB-myc for 24 hours and treated with torin-1 for 4 hours, followed by immunostaining using rabbit anti-myc antibody and mouse anti-rabbit Alexa 594 secondary antibody (ab150128; Abcam, Cambridge, United Kingdom).

Detecting and Tracking Lysosomes in Images

To identify lysosomes in a given image, the Spot Detector plugin of the Icy software (De Chaumont et al., 2012) was used. Cartesian coordinates of detected lysosomes were exported into an Excel XLS file and then imported into our custom MATLAB (MathWorks, Natick, MA) software for further spatial statistical analysis of their distributions. Lysosomes in images from some experiments, especially these conditions with dense lysosome clusters such as trehalose treatment, were detected using custom implementation of a detector based on the algorithm described in (Ponti et al., 2003), which is included in the MATLAB software. To track movement of lysosomes in a given time-lapse video, the Spot Tracking plugin of Icy (Chenouard et al., 2013; De Chaumont et al., 2012) or TrackMate plugin in ImagJ was used. The recovered lysosome trajectories were exported into an Excel XLS file (SpotTracking) or a CSV file (TrackMate), and then imported into our custom software for further mean-square-displacement (MSD) analysis and spatial statistical analysis. Our software is openly available in source code at https://github.com/ccdlcmu/LysosomeSpatialOrganization_code.

Complete Spatial Randomness Test of Lysosomal Distributions

As an essential step in statistical analysis of spatial point processes (Illian et al., 2008), complete spatial randomness (CSR) test was performed on the distribution of lysosomes at the whole-cell scale to check whether it was entirely random. Specifically, for a given cell, its boundary was manually traced using the *imfreehand* function in MATLAB. The boundary geometry data and the coordinates of detected lysosomes were then passed to *R* for calculation of the Ripley's *K*-function by calling the *spatstat* package. To provide a reference for comparison, a homogeneous Poisson point process was simulated in the same cell geometry with the mean number of simulated lysosomes matching the number of actual lysosomes. The *K*-function was calculated from 99 rounds of simulation. Because the *K*-function for a homogeneous Poisson process has the form $K(r) = \pi r^2$ (Illian et al., 2008), where r denotes neighborhood radius, we subtracted πr^2 from the calculated *K*-functions of both actual and simulated lysosomal distributions for convenience of comparison (Fig. 1C-E). Substantial separation of the actual *K*-function from the reference would indicate non-randomness in distribution.

Characterization of Lysosome Distribution at the Whole-Cell Scale

Lysosome distribution at the whole-cell scale was characterized using statistical distributions of distances between individual lysosomes as well as distances between individual lysosomes and the cell nucleus. These distributions were constructed based on the point process theory of spatial statistical analysis (Diggle, 2014; Illian et al., 2008) and were calculated from detected lysosome positions using our custom software.

(Normalized) Inter-organelle distance distribution: For a given cell, the distribution is calculated from all pairwise distances of its lysosomes (Fig. S1A), which characterizes spacing between lysosomes at the whole-cell scale. Specifically, for the i^{th} and j^{th} lysosomes, whose positions are denoted $\left(p_x^i, p_y^i\right)$ and $\left(p_x^j, p_y^j\right)$, respectively, their inter-organelle distance $D_{IO}(i,j)$ is their Euclidean distance, $D_{IO}(i,j) \triangleq \sqrt{\left(p_x^i - p_x^j\right)^2 + \left(p_y^i - p_y^j\right)^2}$, $i \neq j,\ \ i,j \in [1..N]$, where N is the total number of lysosomes. To account for variations in cell sizes, the normalized inter-organelle distance $\tilde{D}_{IO}(i,j) \triangleq D_{IO}(i,j) / D_{IO}^{Max}$ is used, where $D_{IO}^{Max} \triangleq \max\{D_{IO}(i,j)\}$ is the maximum inter-organelle distance. For each cell, after calculating its complete set of normalized inter-organelle distances, $\left\{\tilde{D}_{IO}(i,j),\ i \neq j,\ \ i,j \in [1..N]\right\}$, the

probability density function (pdf) of the distances is estimated using MATLAB function *ksdensity* with default parameters, including a normal kernel whose bandwidth is optimized for density estimation.

(Normalized)To-nucleus distance distribution: For analysis given cell, the boundary of its nucleus (from DAPI-staining or DIC image) is manually traced and then approximated by the set of boundary points using the MATLAB function *imfreehand*. We denote the set of boundary points as $S(C)$. For the i^{th} lysosome, its to-nucleus distance $D_{TN}(i)$ is its distance to the nearest nucleus boundary point, defined as $D_{TN}(i) \triangleq \min_{(s_x^A, s_y^A)\in S(A)} \sqrt{\left(p_x^i - s_x^A\right)^2 + \left(p_y^i - s_y^A\right)^2}$. The normalized to-nucleus distance $\tilde{D}_{TN}(i) \triangleq D_{TN}(i) / D_{TN}^{Max}$ is used to account for variations in cell sizes, where $D_{TN}^{Max} \triangleq \max\{D_{TN}(i)\}$ is the maximum to-nucleus distance. For each cell, the probability density function of its complete set of normalized to-nucleus distances, $\{\tilde{D}_{TN}(i)\}$, $i \in [1..N]$, is estimated using MATLAB function *ksdensity* with the same parameter setting as for the inter-organelle distance distribution.

Nearest-neighbor distance distribution: For a given cell, this distribution is calculated from all nearest neighbor distances of its lysosomes. It characterizes the shortest distances between individual lysosomes at the whole-cell level. Specifically, for the i^{th} lysosome, its nearest-neighbor distance $D_{NN}(i)$ is defined as $D_{NN}(i) \triangleq \min\{D_{IO}(i,j),\ i \neq j,\ j \in [1..N]\}$. The probability density function of the complete set of nearest-neighbor distances, $\{D_{NN}(i),\ i \in [1..N]\}$ is estimated using MATLAB function *ksdensity* with the same parameter setting as for the inter-organelle distance distribution.

Quantification of Differences in Lysosome Distributions at the Whole-Cell Scale

After defining the distance distributions for characterizing lysosome spatial distributions at the whole-cell level, it is often necessary to compare such distributions at two different time points in the same cell or between two different cells. To compare two distance distributions, represented by pdf_i and pdf_j, respectively, we quantified their difference using the following intersection measure (Cha, 2007), also referred to as the Sorensen distance, which quantifies the level of non-overlap between the two distributions.

$$D_{INT}\left(pdf_i, pdf_j\right) \triangleq \frac{\int_0^L \left|pdf_i(x) - pdf_j(x)\right| dx}{\int_0^L pdf_i(x)\,dx + \int_0^L pdf_j(x)\,dx} = \frac{1}{2}\int_0^L \left|pdf_i(x) - pdf_j(x)\right| dx$$

For normalized distance distributions, L equals 1. For non-normalized distance distributions, L equals the larger one of the two maximal distances of the two distributions.

Classification of Lysosomes Based on their Modes of Movement

Trajectories of lysosomes were recovered through single particle tracking as described above. From each trajectory that lasts at least 25 frames, which correspond to 2.4 seconds in imaging, the mean square displacement (*MSD*) function was calculated as described in (Saxton, 1997) with the maximum lag of 24 frames. Because *MSD* is a function of time, we assume the following simplified model:

$$MSD\left(\tau\right)=A\tau^{\alpha}+B$$

in which α can be used to classify different modes of movement (Qian et al., 1991). To determine α, the *MSD* was fitted using the MATLAB function *nlnfit*. The mode of movement of the corresponding lysosome was then classified according to the following table:

α	**Mode of Movement**
$\alpha<0.9$	Constrained diffusion
$0.9\leq \alpha\leq 1.2$	Free diffusion
$\alpha>1.2$	Directed movement

Density-Based Clustering of Lysosomes

To study collective behavior of lysosomes, clusters of lysosomes were identified using a density based clustering algorithm DBSCAN (Ester et al., 1996). Briefly, a lysosome was randomly selected as a seed. The algorithm then searched a circular neighborhood of radius *r* centered at the seed. If the total number of lysosomes in the neighborhood was less than a preset threshold *k*, the seed was excluded as a noise point. If the number equaled or exceeded the threshold *k*, the seed lysosome with its neighbors were considered to be in a high density region and incorporated in a cluster. The incorporated neighboring lysosomes were then set as new seeds. This process was repeated until the number of lysosomes in a new neighborhood fell below threshold *k*. The algorithm repeated this process for the rest of lysosomes not in any cluster. Note that in this way, each cluster has at least *k* lysosomes within a neighborhood of radius *r*. A threshold setting of $k \geq 4$ was recommended for good performance and reasonable computational cost (Ester et al., 1996). We chose a threshold of $k = 5$ to balance stringency of thresholding and sensitivity for identifying small clusters.

To set the neighborhood radius *r* for a given threshold *k*, the spatial densities of lysosomes should be higher than the spatial densities of a random and uniform distribution of lysosomes with the same total number of lysosomes. This distribution was determined through computer simulation. Specifically, for a given cell, 99 simulations were performed using the *spatstat* package function *runifpoint*, which used the rejection method (Illian et al., 2008) to generate a random and uniform point pattern inside the cell geometry, with the number of simulated lysosomes matching the actual number of lysosomes in the cell. The spatial density distribution of the simulated point pattern was then computed using the *spatstat* function *density.ppp*. A threshold spatial density, denoted λ_{thresh} was then set to be 95% of the maximal spatial density from simulation. The search radius was then calculated as $r=\sqrt{k/\pi\lambda_{thresh}}$, with a threshold of $k = 5$. For a time-lapse movie, the simulation was performed based on the number of lysosomes in the first frame. The search radius determined was then used for the rest of the frames.

Controlling Cell Shape Using Patterned Protein Substrates

Cells were grown into defined shapes by culturing them on patterned protein substrates made by micro-contact printing (Azioune et al., 2009; Singhvi et al., 1994; Xia and Whitesides, 1998).

PDMS stamp fabrication: Protein substrate patterns were designed using AutoCAD (Autodesk, San Rafael, CA). A plastic mask with designed circular substrate patterns (68 μm in diameter) was produced by

CAD/ART Services (Bandon, OR) at 10-µm resolution. Master molds were fabricated by spin coating a 4-µm thick layer of SPR 220-3.0 (MicroChem, MA) onto a 2 µm thick coverslip glass (Fisher Scientific, Hampton, NH) followed by UV exposure at 365 nm using a custom made UV illumination system. Polydimethylsiloxane (PDMS) stamps were made by mixing Sylgard 184 (Dow Corning, MI, US) PDMS base with curing agent at the ratio of 1:10, followed by 1 hour defoaming under vacuum and curing for 12-24 hours at 65 °C. Stamps approximately 1 cm × 1 cm in size were cut from the PDMS blocks for micro contact printing (Azioune et al., 2009).

Micro-contact printing of protein substrates: PDMS stamps were sonicated in 75% ethanol for 30 minutes and dried by nitrogen blowing under a laminar hood. The stamps were then coated with 200 µL of 20 µg/ml fibronectin (Thermo Fisher Scientific, Waltham, MA) in PBS and incubated at room temperature for 1 hour. Alexa 594 conjugated fibrinogen (Molecular Probes, Eugene, OR) was added to the fibronectin solution at a final concentration of 8 µg/ml for visualization of printed patterns (Azioune et al., 2009). The stamps were rinsed in deionized water and dried under a laminar hood. The stamps were then placed with the pattern side down on glass surfaces in 35 mm MatTek dishes (Ashland, MA) with 2.0 cm wells. After 1 hour the stamps were removed to release patterned proteins (Palchesko et al., 2012). To prevent cell attachment in unpatterned area, the printed glass surfaces were coated with 0.1 mg/ml of PLL-g-PEG (Surface Solutions, Dübendorf, Switzerland) in PBS for 1 hour and rinsed with PBS for three times.

Cell culture on patterned protein substrates: Dextran-488 labeled BS-C-1 cells were trypsinized 16 hours after labeling and seeded onto patterned substrates. Unattached cells were removed 45-60 min after seeding. Imaging was performed 4-7 hours after seeding.

Testing Whether Distinct Lysosomal Spatial Distributions in Single Cells are a Secondary Effect of Distinct Cell Shapes

To compare the spatial distributions of lysosomes in different cells, we selected the first frame from the time-lapse movie of each cell and compared the three lysosomal distance distributions among all cells in a pairwise fashion (Fig. S2A-C; blue lines) because the distribution within each cell remained stable over time. We found that the three distributions differed significantly in all or most of the pairwise comparisons (Fig. S2D, “unpatterned” columns), indicating that lysosomes maintain distinct spatial distributions in single cells.

To investigate what causes the variations among single cells in their lysosomal distributions, we examined two sources. First, temporal variations of the three distance distributions within single cells, which we refer to as *intracellular* variations, surely contribute to the variations among different cells, which we refer to as *intercellular* variations. Overall, however, we found that the contribution was very small because the average level of intracellular variations was significantly lower than the average level of intercellular variations (Fig. S2E). Second, different cells often exhibit distinct shapes (Fig. S2F). To check whether variations among different cells in their lysosomal distributions are merely a secondary effect of differences in their shapes, we grew cells into approximately the same size and circular shape on patterned protein substrates (Fig. S2G-H; Video S2). We then checked the intercellular variations of the three distance distributions among the patterned cells (Fig. S2A-C; green lines). All or most of the pairwise comparisons of these distributions showed significant differences (Fig. S2D, “patterned” columns). For the normalized inter-organelle distance distribution and the normalized to-nucleus distance distribution, the levels of intercellular variations among patterned cells remained substantial, though significantly lower than among unpatterned cells (Fig. S2I). For the nearest-neighbor distance distribution, there was no significant difference between unpatterned and patterned cells in terms of intercellular variations (Fig. S2I). Taken together, these results show that, although differences in cell shapes contribute to intercellular variations in spatial distributions of lysosomes, such variations in unpatterned cells are not merely a secondary effect of the distinct cell shapes but, instead, are mediated by intrinsic intracellular mechanisms. This further indicates that lysosomes are spatially organized.

Estimating Spatial Density Distributions of Lysosomes

The spatial density distribution of lysosomes within a single cell represent the number of lysosomes per unit area at different locations inside that cell. This distribution was estimated using the *R* package *spatstat* (Baddeley et al., 2016; Baddeley and Turner, 2005). Specifically, for a given cell, with its size measured in micrometers and its shape represented by a polygon, a window of the same size and shape was created using the *R* function *owin*, Lysosomes detected within the cell as described above were used to create a point pattern object using the *R* function *ppp*. The spatial density distribution was then estimated using a kernel-based method by calling the *R* function *density.ppp.* The estimated spatial density distribution $\hat{\lambda}_\sigma(x)$ is defined by the following equation:

$$\hat{\lambda}_\sigma(x) = \frac{1}{N}\sum_{i=1}^{N} K_\sigma(x - x_i), \quad x, x_i \in R^2 ,$$

where $K_\sigma(\cdot)$ is an isotropic 2D Gaussian kernel whose standard deviation σ is also referred to as the bandwidth of estimation, *x* represents any given position within the cell, x_i is the position of the *i*th lysosome, and *N* is the total number of lysosomes in the cell. The grid size for estimating the spatial density distribution was set to be 1 µm. The grid number was determined by the size of the smallest rectangle that circumscribes the cell. No edge correction was performed. Note that the density distribution estimated by *spatstat* is not in the form of a probability density function. Instead, it directly represents the number of lysosomes per unit area and is thus convenient for interpretation.

The estimation bandwidth σ was chosen using the R function *bw.diggle* by minimizing the means squared error of the density estimation (Berman and Diggle, 1989). For estimating spatial density distributions of lysosomes over time in a time-lapse movie, σ was chosen based on the first frame and then kept the same for all subsequent frames.

Immunofluorescence

Cells were grown in 35mm dishes (MatTek, Ashland, MA) and fixed with 4 % formaldehyde for 8 minutes and permeablized in 0.2% Triton X-100/PBS for 5 minutes at room temperature. Cells were then blocked with 5% normal goat serum for 1 hour and incubated with primary antibodies at 4°C overnight and secondary antibodies at room temperature for 1 hour. After each antibody incubation step, cells were washed five times with DPBS with Ca^{2+} and Mg^{2+}, 5 minute each time. Nuclei were then labeled with Hoechst 33342 (Sigma-Aldrich). Samples were imaged in DPBS with Ca^{2+} and Mg^{2+}. To differentiate lysosomes from late endosomes, mouse monoclonal antibody against mannose 6-phosphate receptor

(1:500, Thermo Fisher MA1-066) was used. The secondary antibody used was Alexa Fluor 594-conjugated goat anti-rabbit IgG (1:400, Abcam ab150116, Cambridge, UK).

Calculating ER Spatial Density within Lysosomal Clusters

To study the spatial relations between lysosomal clusters and the ER network, we calculated the local spatial density of the ER network within the clusters. Specifically, ER spatial densities in lysosome cluster regions and non-cluster regions of the same shapes were compared. Here, density is defined by the percentage of pixels occupied by ER inside a region of interest (ROI), $\lambda_{ER} = \frac{N_{pixels\ in\ ROI}}{N_{pixels\ total}} \times 100\ \%$, where $N_{pixels\ in\ ROI}$ denotes the number of pixels belonging to the ER network in a selected region, and $N_{pixels\ total}$ denotes the total number of pixels in the selected region. Clustering of lysosomes were performed with DBSCAN as described above. Cluster boundaries were then detected using MATLAB function *boundary*.

Segmentation of ER: Wide-field fluorescent images of ER were first deconvolved using the software Autoquant (Bitplane, Belfast) to reduce blurring. The deconvolved images were then segmented with a local adaptive thresholding method using MATLAB function *imbinarize* with an input option of 'adaptive'.

Detection of ER densities in lysosome clusters: To obtain ER densities in clustering regions, clustering of lysosomes was performed with the DBSCAN method. Cluster boundaries were then determined using the MATLAB function *boundary*, and the regions within the boundaries were examined in the corresponding ER segmentation results. The pixels with ER signals within a boundary were counted and divided by the total number of pixels within this boundary to obtain the ER density λ_{ER}. To obtain ER densities in non-cluster regions, the cluster boundaries were moved to non-cluster regions, and the ER densities in this non-cluster boundary were then calculated. For each selected cluster boundary, 3-5 non-cluster regions were randomly chosen so that most of the non-cluster regions in a cell were covered. However, this analysis was performed only in regions in which the ER network could be properly segmented.

Analyzing Interactions between Lysosomes and Endosomes

Nearest-neighbor distribution between lysosomes and endosomes: The nearest neighbor distance distribution between lysosomes was extended to characterize the relative positioning of lysosomes with late endosomes. For each lysosome, its distance to the nearest endosome was calculated. Then the probability density function was estimated from the nearest neighbor distance of all lysosomes using MATLAB function *ksdensity* and was referred to as the nearest-neighbor distance distribution between lysosomes and the partner organelles.

Detecting interacting pairs of organelles: Candidates of interacting pairs were detected first based on spatial proximity. A pair of organelle was considered as a candidate if their distance was smaller than a threshold distance $D_{\min}$, which was determined based the following formula

$$D_{\min} = D_{drift} + \max\left(D_{nn}, D_{org}\right).$$

This threshold was calculated for each cell and typically ranged from 0.4 μm to 0.8 μm. D_{drift} denotes the distances organelles travel within the lag of switching between channels during imaging. For the imaging setup of this study, the lag is roughly 1 s, and the corresponding drift was estimated to be ~0.2 μm based on single particle tracking of late endosomes and lysosomes. The nearest neighbor distance D_{nn} was chosen as the lower 10% quantile of the nearest neighbor distance between lysosomes and the partner organelles. Lastly, the diameters of organelles were also considered when D_{nn} is smaller than the lower bound of organelle size D_{org}, which can occur because the position of an organelle was represented by its centroid. The lower bound of organelle size D_{org} was set to be 0.25 μm for COS-7 cells and 0.4 μm for U2OS cells, given the diffraction limit of light microscopy and the fact that late endosomes and lysosomes are often larger than this size.

From the candidate pairs, interacting pairs were identified if the time they stay within the distance threshold is longer than a time threshold. This threshold is set to be 25 seconds based on a >85% quantile of the time different pairs of organelles staying with the distance threshold. The detection results were then visually inspected to exclude errors. Under the distance threshold and the time threshold selected, more than 80% of the detected interacting pairs of lysosomes and endosomes had a spatial overlap of their fluorescence signal during at least 80% of the time they stayed within the threshold distance to each other.

Detecting interacting pairs within organelle clusters: To detect interacting pairs inside organelle clusters, the MATLAB function *boundary* was used to determine boundaries of identified organelle clusters, represented as polygons. Then the function *inpolygon* was used to select interacting pairs. To detect interacting pairs inside overlaying regions of clusters of both types of organelles, endosomes in any interacting pair that lied within or on boundary of any lysosome cluster $C_{lyso}^{(j)},\ j = 1,2, \dots m,$ were detected as candidates. Then the candidate endosomes that fell within or on the boundaries of any endosome cluster(s) were selected. After this step, we accepted the candidate pair if the interacting lysosomes also reside in the same endosome cluster boundary and the lysosome cluster boundary.

Disruption of Lysosome-Endosome Fusion

Knockdown of the HOPS complex in U2OS cells was performed using the on-target Smartpool human Vps39 siRNAs (#9: gcacaaaagaaacgguuca, #10: gcacgacgcuuucgagcca, #11: gugaggagguguuacggau and #12: ggaauacagugcuaguuga) (Dharmacon) by transfecting the cells using the Neon electroporation system. Non-targeting control pool siRNAs (D-001810-10-05, Dharmacon) were used as control. Briefly, around 2×10^5 cells were suspended in a 10 μl pipette tip and electroporated under a pulse voltage of 1230 V, a pulse width of 10 ms, and a pulse number of 4. Following transfection, cells were seeded at $5\text{-}6.7\times10^4$ per 20 mm glass well in 35 mm dishes and incubated for 3 days before imaging. Knockdown of hVps39 mRNA was verified by RT-PCR. mRNA was isolated from cells using TRIzol (Invitrogen) according to the manufacturer's instructions, and converted to cDNA using 2 μg of RNA with the GeneAmp RNA PCR system (Applied Biosystems, Carlsbad, CA). RT-PCR was performed using the T7300 Real Time System (Applied Biosystems, Carlsbad, CA) with 2× SYBR Green (Fermentas, Glen Burnie, MD) and primers (Forward: GAGCCAAAAGCCAACCTCCA; reverse: GCAGAAGGTTGAGGGCCTTG) ordered from Integrated DNA Technologies (Coralville, IA) . cDNA dilutions of 1:15 were used for final qPCR reactions, and 10 µl reactions were run in triplicate on the following parameters: 2 minutes at 50°C, 10 minutes at 95 °C, and 40 cycles at 95 °C for 15 seconds followed by 60 °C for 1 minute.

To determine the disruption of endosome-lysosome fusion, the cells were first incubated with 1.25 mg/ml dextran Alexa 488 for 15 min, and then washed with culture media, followed by lysosome labeling using Magic Red Cathepsin-B (ImmunoChemistry Technologies, Bloomington, MN) at a dilution ratio of 1:1300 (10 times lower than the manufacturer's instructions) for 10 min. Cells were imaged 30 min after washout of the dextran dye. For acute disruption of lysosome-endosome fusion, labeling and BAPTA-AM treatment of U2OS were performed largely according to (Colletti et al., 2012). Briefly, cells were first incubated with 1.5 mg/ml dextran Alexa 488 for 15 min to label late endosomes, and then washed with culture media and treated with 10 µM BAPTA-AM (Merck Millipore, Burlington, MA), followed by lysosome labeling using Magic Red Cathepsin-B. Cells were imaged after 30 min of treatment.

Supplemental References

Azioune, A., M. Storch, M. Bornens, M. Théry, and M. Piel. 2009. Simple and rapid process for single cell micro-patterning. *Lab Chip*. 9:1640-1642.

Baddeley, A., E. Rubak, and R. Turner. 2016. Spatial Point Patterns: Methodology and Applications with R. Chapman & Hall/CRC.

Baddeley, A., and R. Turner. 2005. spatstat: An R package for analyzing spatial point patterns. *J. Stat. Softw.* 12:1-42.

Berman, M., and P. Diggle. 1989. Estimating weightedintegrals of the second-order Intensity of a spatial point process. *J. R. Stat. Soc. Series B Stat. Methodol.* 51:81-92.

Bright, N.A., M.J. Gratian, and J.P. Luzio. 2005. Endocytic delivery to lysosomes mediated by concurrent fusion and kissing events in living cells. *Curr. Biol.* 15:360-365.

Bright, N.A., L. Wartosch, and J.P. Luzio. 2015. Lysosome fusion in cultured mammalian cells. *Methods Cell Biol.* 126:101-118.

Cha, S.-H. 2007. Comprehensive survey on distance/similarity measures between probability density functions. *International Journal of Mathematical Models and Methods in Applied Sciences*. 1:300-307.

Chenouard, N., I. Bloch, and J.C. Olivo-Marin. 2013. Multiple hypothesis tracking for cluttered biological image sequences. *IEEE Trans. Pattern Anal. Mach. Intell.* 35:2736-3750.

De Chaumont, F., S. Dallongeville, N. Chenouard, N. Herve, S. Pop, T. Provoost, V. Meas-Yedid, P. Pankajakshan, T. Lecomte, Y. Le Montagner, T. Lagache, A. Dufour, and J.-C. Olivo-Marin. 2012. Icy: an open bioimage informatics platform for extended reproducible research. *Nat. Meth.* 9:690-696.

Diggle, P.J. 2014. Statistical Analysis of Spatial and Spatiotemporal Point Patterns. CRC Press.

Ester, M., H.-P. Kriegel, #246, r. Sander, and X. Xu. 1996. A density-based algorithm for discovering clusters a density-based algorithm for discovering clusters in large spatial databases with noise. *In* Proceedings of the Second International Conference on Knowledge Discovery and Data Mining. AAAI Press, Portland, Oregon. 226-231.

Griffiths, G., B. Hoflack, K. Simons, I. Mellman, and S. Kornfeld. 1988. The mannose 6-phosphate receptor and the biogenesis of lysosomes. *Cell*. 52:329-341.

Humphries, W.H.t., C.J. Szymanski, and C.K. Payne. 2011. Endo-lysosomal vesicles positive for Rab7 and LAMP1 are terminal vesicles for the transport of dextran. *PLoS One*. 6:e26626.

Illian, J., A. Penttinen, H. Stoyan, and D. Stoyan. 2008. Statistical Analysis and Modeling of Spatial Point Patterns. Wiley.

Kilpatrick, B.S., E.R. Eden, L.N. Hockey, C.E. Futter, and S. Patel. 2015. Chapter 1 - Methods for monitoring lysosomal morphology. *In* Methods Cell Biol. Vol. 126. P. Frances and P. Nick, editors. Academic Press. 1-19.

Luzio, J.P., P.R. Pryor, and N.A. Bright. 2007. Lysosomes: fusion and function. *Nat. Rev. Mol. Cell Biol.* 8:622-632.

Martina, J.A., Y. Chen, M. Gucek, and R. Puertollano. 2012. MTORC1 functions as a transcriptional regulator of autophagy by preventing nuclear transport of TFEB. *Autophagy*. 8:903-914.

Palchesko, R.N., L. Zhang, Y. Sun, and A.W. Feinberg. 2012. Development of polydimethylsiloxane substrates with tunable elastic modulus to study cell mechanobiology in muscle and nerve. *PloS one*. 7:e51499.

Palmieri, M., R. Pal, H.R. Nelvagal, P. Lotfi, G.R. Stinnett, M.L. Seymour, A. Chaudhury, L. Bajaj, V.V. Bondar, and L. Bremner. 2017. mTORC1-independent TFEB activation via Akt inhibition promotes cellular clearance in neurodegenerative storage diseases. *Nat. Commun.* 8:14338.

Ponti, A., P. Vallotton, W. Salmon, C. Waterman-Storer, and G. Danuser. 2003. Computational analysis of F-actin turnover in cortical actin meshworks using fluorescent speckle microscopy. *Biophys. J.* 84:3336-3352.

Porter, K., J. Nallathambi, Y. Lin, and P.B. Liton. 2013. Lysosomal basification and decreased autophagic flux in oxidatively stressed trabecular meshwork cells: implications for glaucoma pathogenesis. *Autophagy*. 9:581-594.

Qian, H., M.P. Sheetz, and E.L. Elson. 1991. Single particle tracking. Analysis of diffusion and flow in two-dimensional systems. *Biophys J*. 60:910-921.

Sarkar, S., J.E. Davies, Z. Huang, A. Tunnacliffe, and D.C. Rubinsztein. 2007. Trehalose, a novel mTOR-independent autophagy enhancer, accelerates the clearance of mutant huntingtin and α-synuclein. *J. Biol. Chem.* 282:5641-5652.

Saxton, M.J. 1997. Single-particle tracking: the distribution of diffusion coefficients. *Biophy J*. 72:1744-1753.

Singhvi, R., A. Kumar, G.P. Lopez, G.N. Stephanopoulos, D.I. Wang, G.M. Whitesides, and D.E. Ingber. 1994. Engineering cell shape and function. *Science*. 264:696-699.

Thoreen, C.C., S.A. Kang, J.W. Chang, Q. Liu, J. Zhang, Y. Gao, L.J. Reichling, T. Sim, D.M. Sabatini, and N.S. Gray. 2009. An ATP-competitive mammalian target of rapamycin inhibitor reveals rapamycin-resistant functions of mTORC1. *J. Biol. Chem.* 284:8023-8032.

Xia, Y., and G.M. Whitesides. 1998. Soft lithography. *Annu. Rev. Mater. Sci.* 28:153-184.